This is a previous version of the article published in Journal of Power Sources. 2019, 412: 451-464. doi:10.1016/j.jpowsour.2018.11.075

MODELING OF OXYGEN REDUCTION REACTION IN POROUS CARBON MATERIALS IN ALKALINE MEDIUM. EFFECT OF MICROPOROSITY

Atsushi Gabe[1], *Ramiro Ruiz-Rosas*[1], *Carolina González-Gaitán*[2], *Emilia Morallón*[2], *Diego Cazorla-Amorós*[1]*

[1] Instituto Universitario de Materiales, Departamento de Química Inorgánica, Universidad de Alicante, Apartado 99, 03080-Alicante, Spain

[2] Instituto Universitario de Materiales, Departamento de Química Física, Universidad de Alicante, Apartado 99, 03080-Alicante, Spain

*Corresponding Author

E-mail address: cazorla@ua.es (D.C.A.).

Postal Address: Universidad de Alicante Carretera de San Vicente del Raspeig s/n 03690 San Vicente del Raspeig Alicante (Spain)

TEL: (+34) 96 590 3400

FAX: (+34) 96 590 3464

Abstract

The role of porosity, and more specifically, microporosity, in the performance of carbon materials as Oxygen Reduction Reaction (ORR) catalysts in alkaline medium still has to be clarified. For this purpose, a highly microporous KOH-activated carbon and a microporous char have been prepared and their ORR performance in alkaline media were compared to that of two commercial carbon blacks with low and high surface areas, respectively. Interestingly, all carbon materials show a two-wave electrocatalytic process, where the limiting current and the number of electron transferred increase when going to more negative potentials. The limiting current and onset potential of the second wave is positively related to the amount of microporosity, and H_2O_2 electrochemical reduction tests have confirmed that the second wave could be related to the catalytic activity towards this reaction. In accordance to these findings, a model is developed that takes into account narrow and wide micropores in both charge transfer reactions and the mass transfer rate of O_2 and H_2O_2. This model successfully reproduces the experimental electrochemical response during ORR of the analyzed porous carbon materials and suggests the important role of narrow micropores in H_2O_2 reduction.

Keywords

Oxygen Reduction Reaction, Hydrogen peroxide reduction, Microporosity, ORR mathematical modeling, Charge transfer reaction, Mass transfer rate

NOMENCLATURE:

$C_{O_2}^b$: oxygen concentration in the bulk of the solution, mol cm^{-3}

C_i^{np}: concentration of *i* component within the narrow micropores of the electrode, mol cm^{-3}

C_i^{wp}: concentration of *i* component within the wide micropores of the electrode, mol cm^{-3}

D_{O_2}: diffusion coefficient of oxygen, $1.8 \cdot 10^{-5}$ cm^2 s^{-1} at 25 ºC

$j_{H_2O_2}$: modeled specific current for the electrochemical reduction of H_2O_2 to H_2O, mA cm^{-2}

j_{O_2}: modeled specific current for the electrochemical reduction of O_2 to H_2O_2, mA cm^{-2}

j_D^{ORR}: modeled specific current on the disk of the rotating ring-disk electrode, mA cm^{-2}

$J_{H_2O_2}^{D,j}$: Hydrogen peroxide internal diffusion rate in narrow or wide micropores, mol cm^{-2} s^{-1}

$J_{H_2O_2}^{K,j}$: intrinsic electrochemical reaction rate for H_2O_2 reduction in narrow or wide micropores, mol cm^{-2} s^{-1}

$J_{O_2}^{D,j}$: Oxygen internal diffusion rate in narrow or wide micropores, mol cm^{-2} s^{-1}

$J_{O_2}^{K,j}$: intrinsic electrochemical reaction rate for O_2 reduction in narrow or wide micropores, mol cm^{-2} s^{-1}

j_{H2O2}^L: Levich limiting current density for hydrogen peroxide, mA cm^{-2}

j_{O2}^L: Levich limiting current density for oxygen, mA cm^{-2}

$k_{H_2O_2}^f$: effective mass transfer coefficient of H_2O_2 within the narrow micropores, cm s^{-1}

$k_{0,i}^{r,j}$: charge transfer rate constant of *i* component at narrow or wide pores, cm s^{-1}

$k_{L,H2O2}^{f}$: mass transfer coefficient of hydrogen peroxide, 0.0074 cm s^{-1} at 1600 rpm

$k_{L,O2}^{f}$: mass transfer coefficient of oxygen, 0.0125 cm s^{-1} at 1600 rpm

k_i^r: kinetic constant for the electrochemical reduction of *i* component, cm s^{-1}

K_i^{ads}: adsorption constant for the *i* component, cm^3 mol^{-1}

α_i: electron transfer coefficient of *i* component

C_g: gravimetric capacitance, F g^{-1}

C_i^j: Concentration of *i* reagent at *j* position (bulk, narrow or wide micropores), mol cm^{-3}

CO_2^{TPD}: CO_2-evolving surface oxygen groups from TPD, μmol g^{-1}

CO^{TPD}: CO-evolving surface oxygen groups from TPD, μmol g^{-1}

C^{XPS}: carbon atomic concentration by XPS, at.%

E: electrode potential vs the reversible hydrogen electrode, V

F: Faraday constant, 96485 C mol^{-1}

I_D: current measured at the disk of the rotating ring-disk electrode, mA

I_R: current measured at the ring of the rotating ring-disk electrode, mA

J: specific current measured on the disk of the rotating ring-disk electrode, mA cm^{-2}

La: crystallite thickness along the a-axis for a graphitic structure, nm

Lc: crystallite thickness along the c-axis for a graphitic structure, nm

n: number of transferred electrons

O^{TPD}: total evolved oxygen from TPD, μmol g^{-1}

O^{XPS}: oxygen atomic concentracion by XPS, at.%

R^{H2O2}: $k^r_{0,H_2O_2}/k^f_{H_2O_2}$ ratio

S_{BET}: apparent surface area from BET method, m^2 g^{-1}

$V_{DR}{}^{CO2}$: Dubinin-Raduskevich micropore volume from CO_2 adsorption isotherm, cm^3 g^{-1}

$V_{DR}{}^{N2}$: Dubinin-Raduskevich micropore volume from N_2 adsorption isotherm, cm^3 g^{-1}

Vmes: mesopore volume from N_2 adsorption isotherm, cm^3 g^{-1}

υ: kinematic viscosity of 0.1M KOH electrolyte, 0.01 cm^2 s^{-1}

ω: rotation rate, rad s^{-1}

η: electrode overpotential, V

ψ: ratio between effective surface area and geometric surface area of disk

*: active site for ORR

*f: free amount of active site

*t: total number of active sites

*(i): adsorbed ORR intermediate on active site

1. INTRODUCTION

Due to their low cost, high stability, high electrical conductivity and tunable surface chemistry and porosity, carbon materials are attractive materials for their use in the formulation of catalysts for electrochemical energy conversion [1]. In the case of low temperature fuel cells, carbon materials are the main component of the electrodes, where they can be employed as a support and, more recently, even as catalyst by themselves. Nowadays, carbon black currently constitutes the preferred support in commercial carbon catalyst layers [2,3].

Much attention is being paid to the development of novel catalysts for the oxygen reduction reaction (ORR) because it is a slow reaction that necessitates high Pt loadings. This reaction takes place at the cathode of all fuel cell systems and other energy storage devices such as metal-air batteries. The high cost, low chemical stability and performance of current platinum-based electrodes are one of the main obstacles for the commercial implementation of these systems, therefore explaining the growing interest in non-noble or metal-free ORR catalysts [4–7]. Even in the case of noble-metal based catalysts, the contribution of carbon support to ORR is far from being negligible, and can account for values as high as one third of the power delivered by a fuel cell [8], and can severely decline the stability of the cathode and the membrane when the 2-electron pathway towards hydrogen peroxide prevails [9]. This explains the huge interest in determining the parameters that drives the ORR activity of carbon materials. The ORR activity of undoped carbon materials is low. The highest activity is achieved at high pH values, although the reaction rate still is sluggish, and the reaction pathway delivers the formation of hydroperoxide ion through a 2-transferred electron process [10]. Nevertheless, the surface chemistry and the textural parameters of carbon materials can be modified for enhancing their electrocatalytic activity.

The effect of the surface chemistry on the ORR activity has been profusely studied in recent years. [5,11,12]. [13]. [14], and a great attention has been devoted to understand the effect of the surface chemistry on the catalysis of ORR by carbon materials and to reveal the nature of the active site [9,11,14–21].

However, the effect of porosity on the kinetics of oxygen reduction by carbon materials is often ignored, and the presence of catalytic species has made challenging any clear assessment [22–27]. Thus, few works can be found where a systematic approach for assessing the role of microporosity of bare carbon materials is reported. In this sense, Appleby and Marie reported ORR kinetic studies carried out on a large collection of carbon materials in alkaline solution [28]. They found that ORR activity increased linearly with BET surface area for carbon blacks, whereas no clear trend was found in the case of activated carbons (ACs). They argued that, even though the high surface area of ACs should provide a larger amount of active sites for ORR, those lying on micropores are unreachable either for the electrolyte (unwetted pores), for dissolved oxygen or for the solvated HO_2^- anion, explaining why their catalytic activity is actually lower than expected considering their BET surface areas. Recently, Liu et al. analyzed the influence of micro and mesoporosity on ORR cathode catalysts [29], and they concluded that activity increases by the presence of microporosity and that mesoporosity is necessary to facilitate accessibility to active sites. On the other hand, Seredych et al. prepared ORR catalysts using a hydrophobic ultramicroporous carbon made from furfuryl alcohol and tannin [30]. The ORR experiments in rotating disk electrode revealed an inverse relationship between the micropore size and volume (especially those with sizes lower than 0.7 nm) and the catalytic activity at low potentials. The authors proposed that a strong adsorption of oxygen takes place in hydrophobic ultramicropores, leading to weakening of O-O bonds and promoting the

dissociation of dioxygen. Again, the presence of a wider porosity of hydrophilic character is considered critical for achieving a good oxygen mass transfer rate to the ultramicropores. Finally, Qu reported the ORR catalytic activity of several ACs of different micropore sizes [31]. However, most of the work is devoted to find a relationship between the activated carbon structure and crystallinity rather than in the effect of microporosity, which is considered to be "not in use" in the gas diffusion layers of catalysts.

This work presents a study of the effect of porosity, and in particular microporosity, in carbon material electrodes in the ORR in alkaline conditions. For this purpose, several carbon materials with different textural properties but similar surface chemistry have been selected. This collection includes a highly microporous activated carbon, a char with a low microporosity development and two commercial carbon blacks of different surface area and pore size distributions. After determining the ORR activity of these materials, a kinetic model for the oxygen reduction reaction over porous carbon materials that takes into account the critical role of microporosity in the ORR mechanism is drawn. In accordance to this model, the current density of porous carbon materials in ORR is derived and its validity for describing the experimental results of the porous carbon samples is discussed.

2. EXPERIMENTAL SECTION

2.1. Material synthesis

A highly microporous activated carbon (KUA) was prepared by chemical activation of Spanish anthracite with KOH. The impregnation ratio of KOH to carbon precursor has been set to 4:1. The activation has been carried out at 750 ºC (heating rate: 5 ºC /min, holding time: 2 hours) in a tubular furnace equipped with a quartz tube feed with 800 mL/min of nitrogen (99.999 %, Air

Liquide). The pyrolyzed mixture was thoroughly stirred in 5 M HCl and distilled water until neutral pH was achieved. The resulting activated carbon was recovered by filtration and dried at 120 ºC. More details about the preparation procedure can be found elsewhere [32]. Microporous char (AC) was prepared by carbonization of a phenolformaldehyde polymer resin in N_2, at 5 ºC /min to 1273 ºC with 1 h soaking time. Commercial Vulcan XC-72F carbon black (XC72) from Cabot corporation and CD-6008 carbon black (CB) supplied from COLUMBIAN CHEMICALS have been used as received.

2.2. Material characterization

The porosity of the carbon materials was analyzed by CO_2 and N_2 adsorption isotherms at 0 ºC and -196 ºC, respectively, using an Autosorb-6B apparatus (Quantachrome). The structure of the samples was characterized by transmission electron microscopy (TEM) and X-ray Diffraction (XRD). The surface chemistry was assessed using X-Ray Photoelectron Spectroscopy (XPS) and Temperature Programmed Desorption (TPD) experiments. More details are in the electronic supplementary information (ESI).

2.3. ORR activity experiments

Electrochemical activity tests towards ORR were conducted at 25 ºC in a thermostated three-electrode cell filled with 0.1 M KOH solution using a Autolab 302N potentiostat (Metrohm). Further explanation about this experiment is in ESI. The number of electrons transferred in the oxygen reduction reaction (n) has been followed during the LSV measurements from the oxidation of hydrogen peroxide over the platinum ring disk using the following equation:

$$n = \frac{4 \cdot I_D}{I_D + I_R/N} \qquad \textbf{(1)}$$

Where I_R and I_D stand for the currents measured at the ring and the disk, respectively, and N is the collection efficiency of the ring, which was experimentally determined to be 0.37. The number of electrons has also been determined from the slope of the Koutecky -Levich plots at different potentials [33] using LSV recorded at several rotation rates (400, 625, 900, 1225 and 1600 rpm).

The limiting current during RDE experiments (j_{O2}^{L}, mA cm^{-2}) has been defined in accordance to Levich model for RDE [33]:

$$j_{O_2}^{L} = n \cdot F \cdot 0.62 \cdot D_{O_2}^{2/3} \cdot \upsilon^{-1/6} \cdot \omega^{1/2} \cdot C_{O_2}^{B} = n \cdot F \cdot k_{L,O_2}^{f} \cdot C_{O_2}^{B} \quad \textbf{(2)}$$

In Eqn. 2, *n* is the number of electrons transferred, *F* is the Faraday constant (96485 C mol^{-1}), D_i is the diffusion coefficient of oxygen ($1.95 \cdot 10^{-5}$ cm^2 s^{-1}), υ is the kinematic viscosity of the solution (0.01 cm^2 s^{-1}) and ω is the rotation rate (rad s^{-1}). The parameters $0.62 \cdot D_{O_2}^{2/3} \cdot \upsilon^{-1/6} \cdot \omega^{1/2}$ have been so-called mass transfer coefficient of oxygen, k_{L,O_2}^{f}, having a value of 0.0125 for 1600 rpm. The oxygen concentration in the solution, $C_{O_2}^{B}$, has a value of $1.2 \cdot 10^{-6}$ mol cm^{-3}. Finally, additional LSV experiments in N_2- and O_2-saturated 0.1 M KOH solution containing 3 mM H_2O_2 were performed using the RDE using the same experimental conditions reported for the ORR experiments.

3. RESULTS AND DISCUSSION

3.1. Characterization of porosity and structure

Figure 1A) compiles the N_2 adsorption-desorption isotherms at -196 ºC for all the carbon materials. The samples have different porosities, as can be visualized from the shape of the adsorption isotherms. Thus, KUA sample shows a type I isotherm according to IUPAC

classification, which is characteristic of microporous solids [34], as well as the highest N_2 uptake. The rounded knee at low relative pressures (0-0.2) points out the presence of a wide micropore size distribution. AC shows a type I plus type IV isotherm shape, with a much lower N_2 uptake than KUA. The hysteresis loop on the desorption branch of the isotherm evidences the presence of mesopores. CB sample also exhibits a combination of type I and IV isotherms although with a large mesoporosity development. Finally, XC72 sample shows a type II isotherm, typical of non-porous solids where multilayer adsorption takes place in the external surface of the particles.

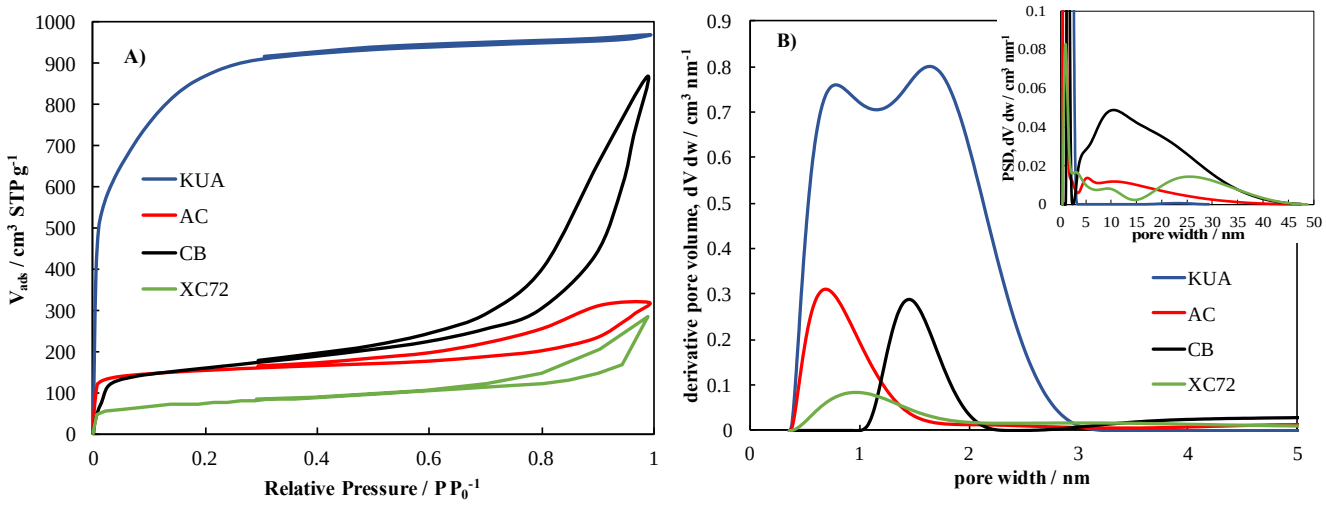

Figure 1. A) N_2 adsorption-desorption isotherms at -196 ºC and B) derived NL-DFT pore size distributions of KUA, AC, CB, and XC72.

Table 1 summarizes the porosity parameters of all the samples. In the case of XC72 and CB, most of the surface area (S_{BET} in **Table 1**) comes from the external surface of the carbon black particles, since the contribution of microporosity is small when compared to the total pore volume of the sample (less than 25%). KUA has a well-developed microporosity (V_{DR}^{N2} in **Table 1**) and also presents a certain amount of mesopores (V_{meso} in **Table 1**) [32,35]. AC and CB share similar V_{DR}^{N2} and S_{BET} values, but the mesoporosity development is very different, with V_{meso} being 4 times larger in the carbon black sample.

Table 1. Textural and structural parameters of the analyzed samples

Sample	**S_{BET} $m^2\ g^{-1}$**	**V_{DR}^{N2} $cm^3\ g^{-1}$**	**V_{DR}^{CO2} $cm^3\ g^{-1}$**	**V_{meso} $cm^3\ g^{-1}$**	**L_c nm**	**L_a nm**
KUA	3300	1.23	0.72	0.15	0.6	2.6
AC	590	0.24	0.26	0.22	0.9	3.6
CB	580	0.26	0.17	0.88	1.2	3.7
XC72	280	0.11	0.05	0.33	1.5	4.0

As for the pore volumes, AC contains both micropores and mesopores with a larger mesopore contribution than KUA (10% of total pore volume are mesopores for KUA, and 45% for AC). CB also combines micropores and wide mesopores, but with an even larger impact of mesoporosity (more than 60% of total porosity). Finally, XC72 did not present any relevant microporosity. It is important to note that the porosity of CB and XC72 samples, is mainly related with the particle size, with micro- and mesopores resulting from the void spaces between the nanosized particles (see ref. [36] for XC72 and TEM images for CB sample in **Figure S1**). We have also evaluated narrow microporosity (pore sizes lower than about 0.7 nm) by using CO_2 adsorption at 0 ºC [37,38]. The similar micropore volume obtained by N_2 and CO_2 adsorption in AC revealed the presence of a narrow micropore size distribution with sizes around 0.7 nm in this sample, whereas CB and KUA have a larger contribution of wide micropores ($V_{DR}^{N2} > V_{DR}^{CO2}$).

The pore size distributions (PSD) for the materials have been calculated from the N_2 adsorption isotherms using NL-DFT method as proposed by Jagiello and Olivier [39] using SAIEUS© software and are shown in **Figure 1B**. These curves confirmed the wide micropore size distributions for KUA and the narrow micro PSD for the other materials. KUA has most of its porosity covering all the micropore range; however, its wide pore size distribution extends into the narrow mesoporosity region, what explains the origin of the V_{mes} value reported in **Table 1**. In the mesopore region, it is possible to see that AC and the carbon blacks show a broad pore size distribution, with mesopores of around 10 nm being the most frequent ones for AC and CB, and 25 nm for XC72 (see inset of **Figure 1B**).

XRD patterns of all samples have been recorded to provide information about their crystalline structure (**Figure S2**). In agreement with the presence of micropores, a large X-Ray scattering at

low angles (below 10º) is clearly observed in porous carbon samples, being this feature maximized in the case of the highly porous KUA. The lattice parameters have been determined from the (002) and (100) peaks [40] and compiled in **Table 1**. It is possible to see that the carbon blacks have a larger structural ordering than the KOH-activated carbon, showing higher sizes of ordered domains in the parallel and perpendicular directions (L_a and L_c in **Table 1**), whereas AC has an intermediate ordering degree.

3.2. Characterization of surface chemistry

The surface chemistry has been analyzed by XPS and TPD, **Table 2**. The microporous activated carbon has the highest oxygen content, while both carbon blacks show the lower amounts, as can be deduced from the XPS results (see **Table 2**). The absence of relevant amounts of other impurities such as sulfur, boron, iron or other heteroatoms was also confirmed. TPD experiments were performed to analyze the functional oxygen groups on the surface of these materials, **Figure S3**. **Table 2** also summarizes the CO, CO_2 and the total amount of oxygen (O) calculated as CO +2(CO_2). When the evolved amounts are normalized in terms of BET surface area, the amounts of evolved CO_2 are lower in KUA (0.10 μmol m^{-2} for KUA and ca. 0.5 μmol m^{-2} for the rest of samples), and those for CO are higher for AC (values of 0.54, 2.42, 1.00 and 1.05 μmol m^{-2} are found for KUA, AC, CB and XC72, respectively).

Table 2. Surface chemistry of the analyzed samples

Sample	**C^{XPS} at.%**	**O^{XPS} at.%**	**CO^{TPD} μmol g^{-1}**	**$CO_2{}^{TPD}$ μmol g^{-1}**	**O^{TPD} wt.%**
KUA	90.7	8.8	1780	330	3.9
AC	94.2	5.8	1430	340	3.5
CB	97.7	2.3	580	280	1.8
XC72	98.0	2.0	230	120	0.6

3.3. Electrochemical characterization

The electrochemical behavior of the samples was analyzed by cyclic voltammetry in N_2 saturated 0.1M KOH between 0 and 1 V at 50 mV s^{-1} (see discussion in supplementary material and **Figure S4**). Linear sweep voltammetry experiments were also recorded in O_2-saturated electrolyte at 10 mV s^{-1}, **Figure 2.** As potential was decreased from 1.0V to less positive values, all samples showed a reduction peak in presence of O_2 presenting a net reduction current when the CV is compared to that recorded in N_2-saturated electrolyte. Onset potentials (defined as the point where the slope of the CV cathodic scan in O_2-saturated electrolyte starts to deviate from that recorded in N_2-saturated electrolyte) were 0.81 V for XC72 and AC, 0.84V for KUA and 0.83V for CB. Further set of experiments using a rotating ring disk electrode have been performed.

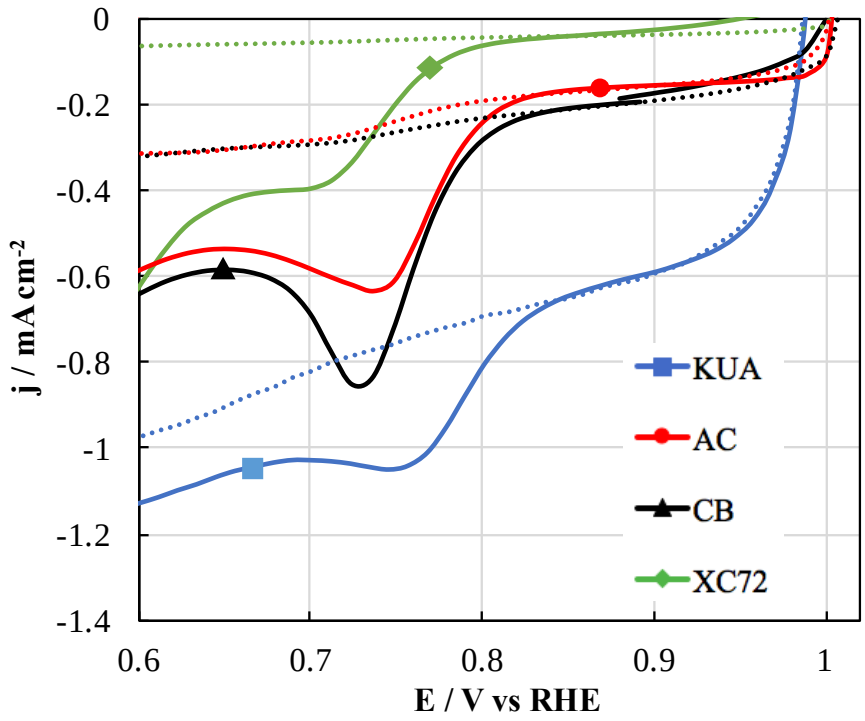

Figure 2. Linear Sweep Voltammetry profiles in N_2- (dashed lines) and O_2- (solid lines) saturated 0.1 M KOH solutions. KUA (blue), AC (red), CB (black) and XC72 (green). Scan rate: 10 mV s^{-1}. Electrode loading: 0.4 mg cm^{-2}

3.4. ORR Rotating ring disk measurements

Figure 3 shows the LSV of all samples at rotation rate of 1600 rpm. The electrodes were stabilized by cycling for 10 minutes in O_2-saturated KOH at 10 mV s^{-1}. After that, the background current was recorded in N_2-saturated electrolyte. The LSV results herein reported were collected after these steps, with the ORR current being corrected by subtraction of the double layer current. The limiting currents for oxygen reduction through 2 and 4 e^- reaction pathways obtained from the Levich theory (2.9 and 5.8 mA cm^{-2} from eqn.2) at the selected experimental conditions are also plotted (dashed grey horizontal lines in **Figure 3A**). The onset potential has been determined at j= -0.1 mA cm^{-2} on the LSV curves in **Figure 3A**. XC72 has the

lowest ORR activity (onset potential of 0.76 V). AC and CB show similar onset potential, 0.80 and 0.79 V, respectively. Remarkably, the activated carbon has a higher onset potential being 0.85 V. Two-wave shape on their LSVs can be observed being less pronounced in the case of KUA and this behavior is found for other carbon materials. These voltammetric profiles are observed independently of the selected rotation rate, **Figure S5**, what demonstrates that this behavior is not related to external mass transfer issues. The same study has been performed using the bare surface of the glassy carbon disk, **Figure S5E, F**, showing that the activity of the disk surface is much lower than that for the tested samples, and it always shows a two-wave shape. Moreover, the diffusion controlled region on the glassy carbon surface starts at potentials lower than 0.3 V, confirming that LSV measurements correspond to the deposited carbon materials.

The number of transferred electrons during ORR has been calculated from the ring to disk current ratio at 1600 rpm and from Koutecky-Levich (K-L) in eqn.1, **Figure 3B**. The ORR activity in these samples involve a 2-electron pathway. An increase on the polarization of the electrode shifts the ORR to a more favorable pathway involving a higher number of electrons (2.4, 2.7, 2.6 and 3.0 at 0.05 V for XC72, CB, AC and KUA samples according to RRDE experiments, and 2.5, 3.1, 2.8 and 3.4 according to K-L theory). The increase in the number of transferred electrons at that potential region seems to be correlated with the presence of microporosity, **Table 1**, rather than with any other textural, structural or surface chemistry parameter. This would be in agreement with recent findings where ORR activity of milled N-doped carbon nanotubes has been reported to increase due to the formation of microporosity [22].

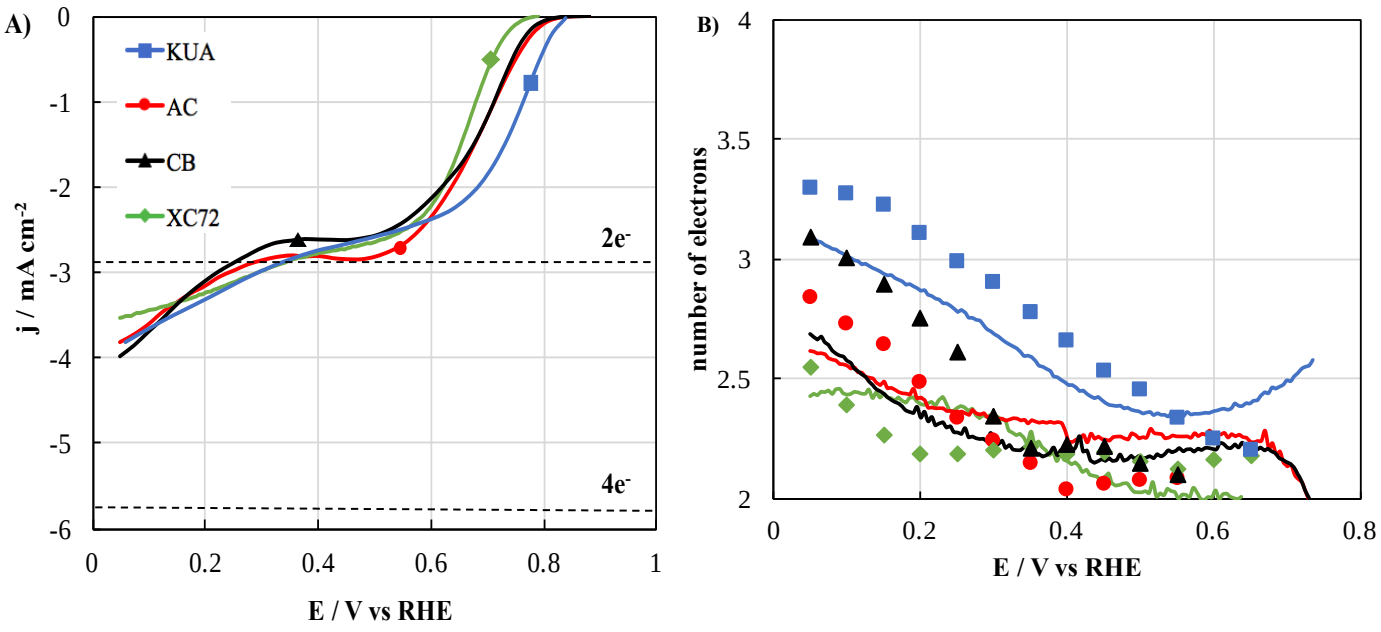

Figure 3. Oxygen reduction reaction study from the RRDE at 1600 rpm in 0.1M KOH solution. A) LSV in the disk electrode (scan rate: 5 mV/s, capacitive currents corrected). B) number of electrons measured from the ring vs disk currents (full lines) and from Koutecky-Levich theory (dots). KUA (blue), AC (red), CB (black) and XC72 (green). Catalyst loading: 0.4 mg cm^{-2}.

3.5. Mass loading effect in ORR

Measurements were conducted using two additional sample loadings (0.10 and 1.00 mg cm^{-2}) for KUA, **Figure S6A, B**. LSV curves have been also expressed in gravimetric terms, **Figure S6C, D**. Both kinetic and diffusion rates are negatively impacted by a low surface loading, as manifested by the current decrease and the onset potential being shifted to less positive potentials at 0.10 mg cm^{-2}. In addition, the shape of the LSV profile becomes similar to that of bare glassy carbon surface at medium and low potentials (see dotted, blue line vs dotted, black line in **Figure S6A**). Decline on ORR activity derived from very low catalyst loading in RRDE experiments

has been reported in the past, and it has been accounted to the catalyst particles being unable to fully cover the whole surface of the disk, rendering a lower effective surface of the electrode [41]. It has been also proposed that a high diffusion film resistance in the electrode could result from excessive thickness, reducing the current density [42]. The effect of the different loadings is easily observed when the LSV profiles are normalized in terms of weight. It can be seen that the normalized current in the vicinity of the onset potential goes through a maximum at medium surface loadings, **Figure S6C**, confirming that kinetic control is reached at that loading, while lower or higher loadings have a negative impact on the ORR activity due to the aforementioned reasons.

Differently, an improvement in the mass transfer rate on the diffusional controlled region (i.e. higher limiting current due to higher oxygen diffusion rate) is observed when raising the loading from 0.40 to 1.00 mg cm^{-2}, **Figure S6A**. The impact of the ratio between the effective surface area available for oxygen diffusion and reduction and the geometrical area of the disk (which is the used one in the Levich theory for determining oxygen diffusion rate on a rotating flat electrode surface) in the oxygen mass transfer rate on RDE measurements has been already exposed in the literature [33,43,44]. At 0.40 mg cm^{-2}, the disk surface is not fully covered by KUA particles. When KUA loading increases, so does the effective area of the electrode. Therefore, the higher current registered in the diffusional controlled region for 1.00 mg cm^{-2}, **Figure S6A**, is in agreement with recent findings regarding an enhanced ORR activity in RDE experiments of porous electrodes and nanoparticles-based catalysts due to a higher effective surface area [43,45,46]. As expected, the gravimetric current values in the diffusional controlled region decrease with the loading of the catalyst, **Figure S6D**. In this region, all oxygen molecules are electrochemically reduced once they reach the electrodic surface, and therefore the

current is only determined by the oxygen diffusional flow towards the electrode and the number of transferred electrons during the reaction (i.e. limiting current is reached).

The number of electrons transferred is positively related to the surface loading, **Figure S6B.** We propose that *n* values between 2 and 4 e^- observed once the diffusion-controlled region is reached, are due to the occurrence of two electrochemical reduction reactions: i) the reduction of the oxygen molecules to hydrogen peroxide, involving two electrons, ii) the reduction of some of the hydrogen peroxide produced in reaction i) to hydroxide, what involves 2 additional electrons. The number of electrons is then determined by the ratio between the H_2O_2 diffusion and electrochemical reaction rates. When the electrochemical reaction rate for H_2O_2 reduction is much higher than the diffusion rate, the number of transferred electrons would be close to 4, whereas a high mobility of H_2O_2 would decrease the contact time with the active sites, and a relevant part of H_2O_2 could diffuse out the surface of the electrode, delivering a number of electrons for ORR close to 2. Then, the presence of micropores (which favour the adsorption of H_2O_2) may increase the residence time of H_2O_2, increasing the probability for further reduction reaction. As KUA loading increases, so does the amount of micropores and residence time of H_2O_2 and, consequently, the H_2O_2 reduction rate.

3.6. Electrochemical reduction of hydrogen peroxide in RRDE

In order to check the validity of this assumption, the electrochemical reduction of H_2O_2 has been analyzed under similar conditions to those employed in ORR measurements in **Figure 3**. The concentration of hydrogen peroxide was 3 mM so that it would be in agreement with the concentration of H_2O_2 in the micropores produced by the 2-electron reduction reaction of O_2. **Figure 4A** compares the LSV curves for all the samples recorded in 3 mM H_2O_2 and N_2-saturated electrolyte. A net reduction current is observed as potential decreases, and the three

porous samples delivered a much higher reduction current than XC72. In addition, the LSVs for hydrogen peroxide reduction share the same potentials intervals as those observed in the transition between the 2 and the 4 electrons pathway detected in **Figures 3 and S6**. The onset potentials for the electrochemical reduction of H_2O_2 follow the order KUA >> CB ~ AC > XC72. This order is similar to that of V_{DR}^{N2}, **Table 1**. The shape of the LSV reveals that no limiting current is achieved in these experiments (Diffusion coefficient of hydrogen peroxide is $0.9 \cdot 10^{-5}$ cm^2 s^{-1}, k^f_{L,H_2O_2} is estimated to be 0.0074 cm s^{-1}, and therefore Levich theory predicts 4.18 mA cm^{-2} at 1600 rpm for 3 mM H_2O_2), probably due to the poor electron transfer rate of active sites located within micropores and the presence of an additional internal mass transfer limitation.

When the ORR activity is determined in the presence of H_2O_2, **Figures 4B-D**, the resulting LSV are in agreement with a linear addition of the profiles for ORR and hydrogen peroxide reduction reactions experiments. Therefore, no competition between H_2O_2 and O_2 for the active sites seems to take place.

The electrochemical reduction of H_2O_2 by porous carbon electrodes has been previously studied. Most works relate this reduction with a longer contact time between the surface of the carbon electrodes and hydrogen peroxide [44,47,48]. It is well known the higher adsorption potential of narrow micropores and their molecular sieve properties [38,49]. The presence of micropores with sizes smaller than 0.7 nm has been related to a higher storage capacity for the electrochemical hydrogen storage [50], and improved capacitance in supercapacitors [51], proving that these pores are active in electrochemical processes. Thus, higher O_2 and H_2O_2 concentrations due to their favorable adsorption in the narrow microporosity of the most active samples (KUA and AC in a lesser degree) could explain the improved catalytic activity.

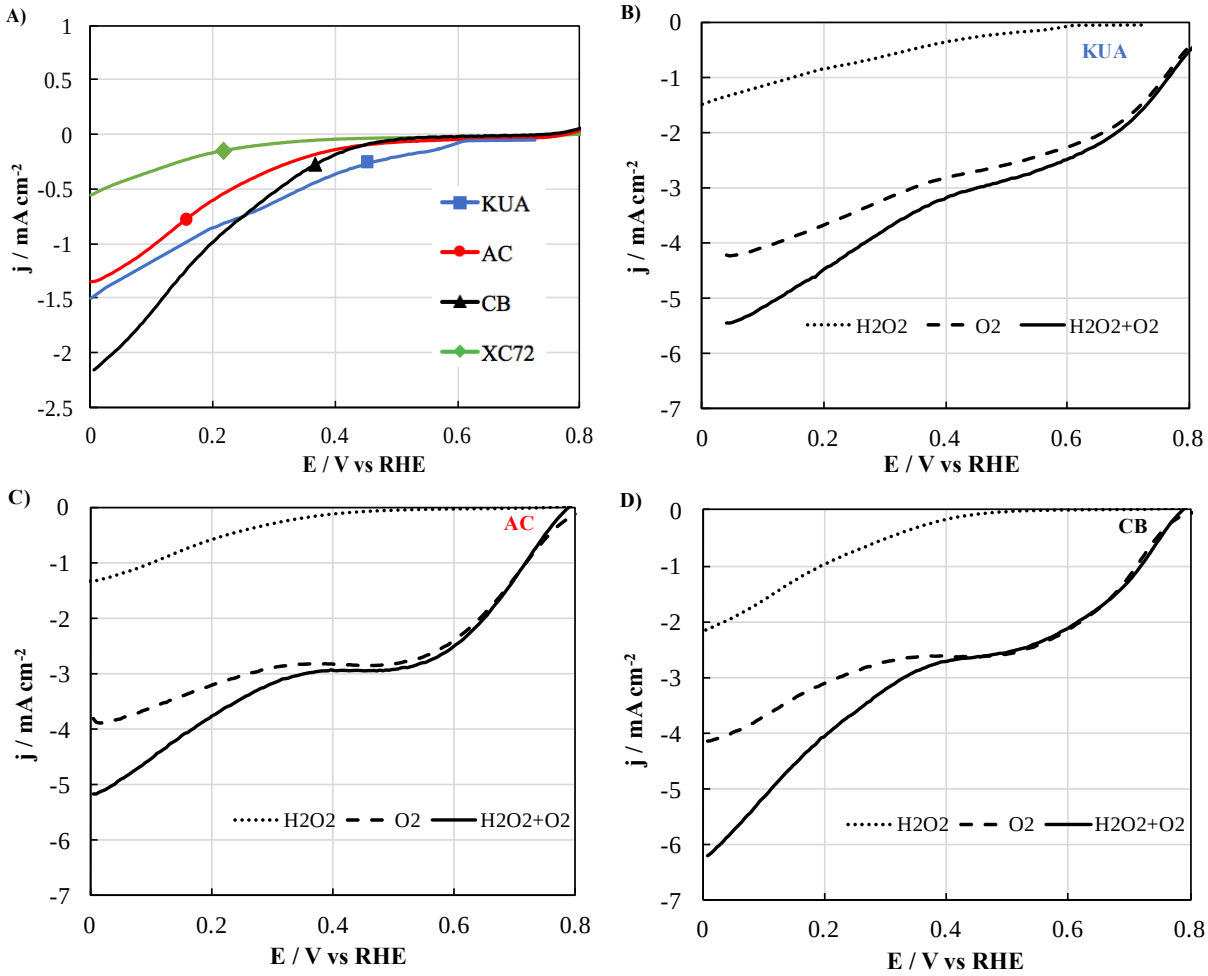

Figure 4. A) LSV profiles of hydrogen peroxide reduction ([H_2O_2]: 3 mM) obtained using RRDE at 1600 rpm in N_2-saturated 0.1M KOH. B) KUA, C) AC and D) CB LSV at 1600 rpm in 0.1 M KOH in H_2O_2 and N_2-saturated electrolyte (dotted lines), H_2O_2 and O_2-saturated electrolyte (solid lines), and O_2-saturated electrolyte (dashed lines).

3.7. Effect of rotation rate on ORR activity

Experiments at different rotation rates have been conducted to discard that H_2O_2 formed during ORR is electrochemically reduced at the external surface of the electrode due to an increased contact time (**Figure S7)**. This premise is derived from the work by Zhou et al., who have recently proposed that ORR of nitrogen-doped carbon materials cannot be properly analyzed using RRDE due to the dependence of hydrogen peroxide concentration at the surface of their catalysts [52]. We have observed that the selectivity towards hydrogen peroxide at less positive potentials is unrelated to the rotation rate or even slightly decreases with the rotation rate (which, in any case, is the opposite behavior to that proposed by Zhou et al.), **Figure S7**. Therefore, the internal diffusion rates of oxygen and hydrogen peroxide, which are independent of the rotation rate, are responsible for the conversion rate of hydrogen peroxide to hydroxide in microporous carbon electrodes.

3.8. Effect of oxygen adsorption time

Seredych et al. recently proposed that the strong adsorption of oxygen in narrow micropores weakens the O-O bond, favoring the oxygen reduction to water via 4-electron pathway at less positive potentials [30]. These micropores are highly hydrophobic and they withdraw oxygen from the electrolyte that is later electrochemically reduced. Nevertheless, oxygen must diffuse through wetted pores before reaching the narrower ones. The low mass transfer rate in wetted pores has been pointed out as the origin of the performance decay of microporous Me-N-C catalysts; as pores get flooded with water formed during ORR, oxygen change its diffusion mode from gaseous diffusion to liquid diffusion through the wetted pores, what results in a higher mass transfer resistance [12]. Therefore, a very low oxygen mass transfer rate is expectable. In this sense, we have checked if ORR activity increases due to a higher local concentration of O_2 within the pores. For that purpose, **Figure S8** compares the LSV ORR profile at 1600 rpm of

KUA recorded right after a previous LSV experiment and after 12 hours of O_2 bubbling. If oxygen has diffusive limitations through narrow micropores, the additional adsorption time of 12 hours should render a higher reduction current due to a larger O_2 concentration in the pores. Contrarily, the LSV profiles for both experiments are fairly similar, so either the oxygen concentration within narrow micropores is not playing a relevant effect, or all the active sites hosted in these micropores can be reached by oxygen in short times. Consequently, hydrogen peroxide reduction to water at micropores, rather than the direct oxygen reduction to water, is considered the prevailing mechanism behind the improved ORR activity shown by porous carbon electrodes at less positive potentials.

3.9. Structural order and ORR activity

The higher ORR activity of microporous activated carbons has been studied by Qu and it has been connected to their structural order parameters derived from XRD [31]. In the case of the porous carbons studied in this work, it is quite straightforward that the relationship between order-related parameters calculated from the XRD profiles, as those compiled in **Table 1**, and ORR activity is not found (i.e., see the well-defined and intense (002) peak of XC72 and the almost absent peak in KUA, **Figure S2**, whereas ORR activity is higher in KUA). Nonetheless, a higher concentration of edge sites is in general expectable in microporous activated carbons, so the identification of edge sites as an active site for ORR could be valid [2], and, in fact, it has been claimed elsewhere [9,21,47,53–55].

3.10. Modeling of ORR in porous carbon materials

The kinetic rate of oxygen reduction reaction relies on the reaction mechanism, which is highly elusive owing to the high irreversibility of the reaction. It has been described for platinum and

other metals [56], but still is far from being proven in the case of carbon materials. The following set of reactions is generally accepted for explaining the hydrogen peroxide pathway in alkaline solutions [9,10,57]. In it, oxygen adsorption on a free active site, $*_f$, is followed by four consecutive surface reactions

$$\boldsymbol{O_2} + *_f \overset{K^*_{O_2}}{\longleftrightarrow} *(\boldsymbol{O_2}) \quad \textbf{(3)}$$

$$*(\boldsymbol{O_2}) + \boldsymbol{e^-} \overset{k^{r1}_{O_2}}{\longrightarrow} *(\boldsymbol{O_2}^-) \quad \textbf{(4)}$$

$$*(\boldsymbol{O_2}^-) + \boldsymbol{H_2O} + \boldsymbol{e^-} \overset{k^{r2}_{O_2}}{\longrightarrow} *(\boldsymbol{HO_2}^-) + \boldsymbol{OH^-} \quad \textbf{(5)}$$

$$*(\boldsymbol{HO_2}^-) + \boldsymbol{H_2O} + \boldsymbol{e^-} \overset{k^{r1}_{H_2O_2}}{\longrightarrow} *(\boldsymbol{OH}\cdot) + \boldsymbol{2OH^-} \quad \textbf{(6)}$$

$$*(\boldsymbol{OH}\cdot) + \boldsymbol{e^-} \overset{k^{r2}_{H_2O_2}}{\longrightarrow} *(\boldsymbol{OH^-}) \quad \textbf{(7)}$$

Both hydroperoxide and hydroxide anions can desorb from the active site, explaining the intermediate *n* values between 2 and 4 e-

$$*(\boldsymbol{HO_2}^-) \overset{K^p_{H_2O_2}}{\longleftrightarrow} \boldsymbol{HO_2}^- + *_f \quad \textbf{(8)}$$

$$*(\boldsymbol{OH^-}) \overset{K^p_{OH^-}}{\longleftrightarrow} \boldsymbol{OH^-} + *_f \quad \textbf{(9)}$$

Considering steady state approximation for the adsorbed superoxide anion and hydroxyl species in Eqn. 4-7 and the adsorption constants, Eqn. 3, 8 and 9, the * site balance can be solved. It allows to define the electrochemical reaction rates, J^K (mol cm^{-2} s^{-1}) of oxygen and hydrogen peroxide supposing that the rate determining steps are the formation of the superoxide anion and the reduction of the hydroperoxide anion

$$J_{O2}^{K} = -k_{O_2}^{r1} \cdot C_{*(O_2)} = \frac{-(k_{O_2}^{r1} \cdot C_{*_t}) \cdot K_{O_2}^{ads} \cdot C_{O_2}}{1+\left(1+\frac{k_{O_2}^{r,1}}{k_{O_2}^{r,2}}\right) \cdot K_{O_2}^{ads} \cdot C_{O_2} + \left(1+\frac{k_{H_2O_2}^{r,1}}{k_{H_2O_2}^{r,2}}\right) \cdot 1/K_{H_2O_2}^{ads} \cdot C_{HO_2^-} + 1/K_{OH^-}^{ads} \cdot C_{OH^-}} \quad \textbf{(10)}$$

$$J_{H_2O_2}^{K} = k_{O_2}^{r1} \cdot C_{*(O_2)} - k_{H_2O_2}^{r1} \cdot C_{*(HO_2^-)} = \frac{(k_{O_2}^{r1} \cdot C_{*_t}) \cdot K_{O_2}^{ads} \cdot C_{O_2} - (k_{H_2O_2}^{r1} \cdot C_{*_t}) \cdot \frac{1}{K_{H_2O_2}^{ads}} \cdot C_{HO_2^-}}{1+\left(1+\frac{k_{O_2}^{r,1}}{k_{O_2}^{r,2}}\right) \cdot K_{O_2}^{ads} \cdot C_{O_2} + \left(1+\frac{k_{H_2O_2}^{r,1}}{k_{H_2O_2}^{r,2}}\right) \cdot \frac{1}{K_{H_2O_2}^{ads}} \cdot C_{HO_2^-} + \frac{1}{K_{OH^-}^{ads}} \cdot C_{OH^-}} \quad \textbf{(11)}$$

The detailed mathematical derivation of the concentration of free sites is presented in the EIS. Note that the kinetic constants (k_i^r) are potential-dependent, in agreement to the Butler-Volmer model [33]

$$k_i^r = k_{0,i}^r \cdot exp(-\alpha_i \cdot f \cdot \eta) \quad \textbf{(12)}$$

Previous studies have also reported first-order kinetics for the reduction of oxygen in carbon electrodes [57]. Similarly, hydrogen peroxide reduction experiments on AC, CB and KUA point out a linear increase of the current for [H_2O_2] of 2 and 3 mM, Figure S9. Considering Equations 10 and 11, first order kinetics for oxygen or hydrogen peroxide reduction is attained when the term $\frac{1}{K_{OH^-}^{ads}} \cdot C_{OH^-}$ prevails over $\left(1+\frac{k_{O_2}^{r,1}}{k_{O_2}^{r,2}}\right) \cdot K_{O_2}^{ads} \cdot C_{O_2} + \left(1+\frac{k_{H_2O_2}^{r,1}}{k_{H_2O_2}^{r,2}}\right) \cdot \frac{1}{K_{H_2O_2}^{ads}} \cdot C_{HO_2^-}$. This scenario is likely to happen in alkaline electrolyte, where hydroxide concentration is several orders of magnitude higher than oxygen and hydrogen peroxide ones. In agreement with this observation, the relevance of hydroxide concentration in the kinetic rate of ORR on carbon materials has been confirmed by Yang and McCreery [10]. The reduction experiments performed in presence of both O_2 and H_2O_2 also revealed the absence of competitive adsorption, Figure 4, confirming that the adsorbed amount of H_2O_2 does not affect the kinetic rate at the studied conditions. Thus, since the number of parameters for fitting would be very high and the catalysts under study are low crystallinity materials with a high heterogeneity and information regarding

the nature and structure of the active sites is not well known, what is an important difference compared to highly crystalline materials like Pt based catalysts [56], we will use in this study first order kinetics. This will permit us to deepen into the role of the microporosity in these materials. Considering first order kinetic rates, simplified expressions for the 2+2 reaction pathway could be derived as follows

$$\boldsymbol{J_i^{K,j} = -k_i^{r,j} \cdot C_i^p = -k_{0,i}^{r,j} \cdot exp(-\alpha_i \cdot f \cdot \eta) \cdot C_i^p} \quad \textbf{(13)}$$

Where $k_{0,i}^{r,j}$ is the charge transfer rate constant ($cm \cdot s^{-1}$) for the reduction reaction of the *i* reagent (either O_2 or H_2O_2) in the narrow or wide micropores (being j=n and j=w, respectively). Note that this parameter is assumed to include adsorption constants, amount of active sites and the rest of terms included in the denominator of Eqn. 10 and 11. α_i is the electron transfer coefficient, η is the overpotential (V) and C_i^p stands for the concentration ($mol \cdot cm^{-3}$) of the *i* reagent in the pores involved in the reduction reaction. Standard potentials of 1.17 V / vs NHE for ORR and 0.935 V / vs NHE for H_2O_2 reduction reaction at pH 13 have been considered for calculating the overpotential. Furthermore, f stands for F/RT, where R is gas constant (8.314 J K^{-1} mol^{-1}) and T is the temperature (25 ºC).

Once the kinetic rate expression is defined, it must be coupled with the mass transfer rates. According to our experimental data, the presence of micropores can have an influence in the residence time of the reactants and reaction products through internal diffusional limitations. We present a model to describe the ORR in porous carbons under the following assumptions.

- Narrow and wide micropores can have different mass transfer rates, J_D, and density of active sites, $\boldsymbol{C_{*_t}}$. The latter value is numerically included within the charge transfer rate constant, ($\boldsymbol{k_{0,i}^{r,j} \cdot C_{*_t}}$). Hence $\boldsymbol{k_{0,i}^{r,j}}$ will show different values for the wider and the narrow

pores during the parameter optimization. Oxygen and hydrogen peroxide concentration will also differ for narrow ($C_{O_2}^{np}$ and $C_{H_2O_2}^{np}$, mol cm^{-3}) and wide micropores ($C_{O_2}^{wp}$ and $C_{H_2O_2}^{wp}$, mol cm^{-3}).

- The limiting diffusion rates at the outer surface of the electrodes ($J_{O_2}^{L}$ and $J_{H_2O_2}^{L}$, mol cm^{-2} s^{-1}) are governed by the RDE theory and can therefore be predicted in accordance to Eqn. 2.
- Oxygen mass transfer rates, $J_{O_2}^{D,n}$ and $J_{O_2}^{D,w}$, are ruled by the RDE theory, since no additional mass transfer limitations have been found for ORR, Figure S8. Narrow and wide micropores are supposed to be randomly distributed in carbon particles, so that the entrances of the pores are equally accessible to oxygen, ruling out the prerequisite of oxygen diffusing through wider pores before reaching the narrower ones. However, they will differ in ψ, the parameter representing the ratio between the effective surface area for mass transfer of narrow or wide micropores with respect to the geometrical surface area of the disk. In this sense, the higher volume of each porosity type, the larger the effective surface area available for diffusion in that porosity

$$\boldsymbol{J_{O_2}^{D,n}} = \psi_n \cdot \boldsymbol{k_{L,O_2}^{f}} \cdot \left(\boldsymbol{C_{O_2}^{b}} - \boldsymbol{C_{O_2}^{np}}\right) \quad \textbf{(14)}$$

$$\boldsymbol{J_{O_2}^{D,w}} = \psi_w \cdot \boldsymbol{k_{L,O_2}^{f}} \cdot \left(\boldsymbol{C_{O_2}^{b}} - \boldsymbol{C_{O_2}^{wp}}\right) \quad \textbf{(15)}$$

$k_{L,O2}^{f}$is the mass transfer coefficient of oxygen according to the RDE theory, having a value of 0.0125 cm s^{-1} for 1600 rpm.

- The produced hydrogen peroxide in wide micropores can diffuse outside the porosity of the electrode following the same diffusion mechanism as oxygen, i.e. a linear driving force model:

$$\boldsymbol{J_{H_2O_2}^{D,w}} = \psi_w \cdot \boldsymbol{k_{L,H_2O_2}^{f}} \cdot \left(\boldsymbol{C_{H_2O_2}^{wp}} - \boldsymbol{C_{H_2O_2}^{b}}\right) \quad \textbf{(16)}$$

k_L^f is the limiting mass transfer coefficient of hydrogen peroxide showing a value of 0.0069 cm s^{-1} at 1600 rpm. Given the large volume of the cell, the low formation rate of hydrogen peroxide and the short analysis times, the bulk concentration of hydrogen peroxide, $C_{H_2O_2}^b$, can be considered negligible.

- Hydrogen peroxide reduction has shown additional mass transfer limitations in these carbon materials, Figure 4. In accordance, the mass transfer rate in narrow pores will be defined using the same expression as the previous diffusional fluxes, but the mass transfer coefficient for narrow micropores, $\boldsymbol{k_{np,H_2O_2}^{f}}$ is taken as a model parameter that is expected to have a lower value than that predicted for H_2O_2 from the RDE theory

$$\boldsymbol{J_{H_2O_2}^{D,n}} = \psi_{np} \cdot \boldsymbol{k_{np,H_2O_2}^{f}} \cdot \left(\boldsymbol{C_{H_2O_2}^{np}}\right) \quad \textbf{(17)}$$

This equation can be understood as a film diffusion resistance, where $k_{np,H2O2}^f$ is taking the role of the ratio between the diffusion coefficient and the film thickness [33].

- The current registered at the disk ($\boldsymbol{j_D^{ORR}}$, mA cm^{-2}) is produced by the electrochemical reduction of oxygen to hydrogen peroxide (2 e^-, $\boldsymbol{j_{O_2}}$) and the electrochemical reduction of hydrogen peroxide to hydroxide (2 e^-, $\boldsymbol{j_{H_2O_2}}$).

$$\boldsymbol{j_D^{ORR}} = \boldsymbol{j_{O_2}} + \boldsymbol{j_{H_2O_2}} \quad \textbf{(18)}$$

- The effective number of electrons transferred (*n*) can be estimated from the ratio between the reduction currents of oxygen and hydrogen peroxide (i.e. when all the produced hydrogen peroxide is further reduced to hydroxide, the overall number of transferred electrons is 4):

$$\boldsymbol{n} = \boldsymbol{2} \cdot \left(\boldsymbol{1} + \frac{\boldsymbol{j_{H_2O_2}}}{\boldsymbol{j_{O_2}}}\right) \quad \textbf{(19)}$$

- The electrochemical reaction rates are those defined in Eqn. 10 and 11 for the full kinetic mechanism, and those from Eqn. 12 for the simplified kinetic mechanism.
- The intrinsic electrochemical reaction rates for O_2 and H_2O_2 reduction (respectively denoted as $\boldsymbol{J_{O_2}^K}$ and $\boldsymbol{J_{H_2O_2}^K}$, mol cm^{-2} s^{-1}) are related to the disk current through the number of electrons transferred (2 e$^-$) and the Faraday constant, F (96485 C mol^{-1} e^{-1}):

$$\boldsymbol{j_D^{ORR} = j_{O_2} + j_{H_2O_2} = 2 \cdot F \cdot (J_{O_2}^{K,n} + J_{O_2}^{K,w} + J_{H_2O_2}^{K,n} + J_{H_2O_2}^{K,w})} \quad \textbf{(20)}$$

- O_2 and H_2O_2 concentrations in narrow and wide micropores are estimated from their mass balances assuming that quasi-equilibrium conditions are achieved:

$$\boldsymbol{J_{O_2}^{D,w} = J_{O_2}^{K,w} \;\therefore C_{O_2}^{wp} = \frac{\psi_w \cdot k_{L,O_2}^f \cdot C_{O_2}^b}{\psi_w \cdot k_{L,O_2}^f + k_{O_2}^{r,w}}} \quad \textbf{(21)}$$

$$\boldsymbol{J_{O_2}^{D,n} = J_{O_2}^{K,n} \;\therefore C_{O_2}^{np} = \frac{\psi_n \cdot k_{L,O_2}^f \cdot C_{O_2}^b}{\psi_n \cdot k_{L,O_2}^f + k_{O_2}^{r,n}}} \quad \textbf{(22)}$$

$$\boldsymbol{J_{O_2,p}^{K,w} = J_{H_2O_2}^{K,w} + J_{H_2O_2}^{D,w} \therefore C_{H_2O_2}^{wp} = \frac{k_{O_2}^{r,w} \cdot C_{O_2}^{wp}}{k_{H_2O_2}^{r,w} + \psi_w \cdot k_{L,H_2O_2}^f}} \quad \textbf{(23)}$$

$$\boldsymbol{J_{O_2,p}^{K,n} = J_{H_2O_2}^{K,n} + J_{H_2O_2}^{D,n} \therefore C_{H_2O_2}^{np} = \frac{k_{O_2}^{r,n} \cdot C_{O_2}^{np}}{k_{H_2O_2}^{r,n} + \psi_n \cdot k_{np,H_2O_2}^f}} \quad \textbf{(24)}$$

- The model parameters are those defining the intrinsic reaction constants, i.e. $k_{0,O_2}^{r,w}$, $k_{0,H_2O_2}^{r,w}$, $k_{0,O_2}^{r,n}$, $k_{0,H_2O_2}^{r,n}$, α_{O_2} and $\alpha_{H_2O_2}$, and those related with mass transfer rates, i.e. ψ_w, ψ_n and $k_{np,H_2O_2}^f$. However, a linear relationship was found between $k_{np,H_2O_2}^f$ and $k_{0,H_2O_2}^{r,n}$ what means that the same fitting can be reached by keeping constant the ratio between these parameters. The existence of this linear relationship is checked when **Eqn. 17** and **24** are combined. Therefore, the optimization parameters were cut down to eight, with the new combined parameter being $R_{H_2O_2} = k_{0,H_2O_2}^{r,n} / k_{np,H_2O_2}^f$. These parameters are

optimized to minimize the square difference between the experimentally measured current densities and those predicted by the model (**Eqn. 18**).

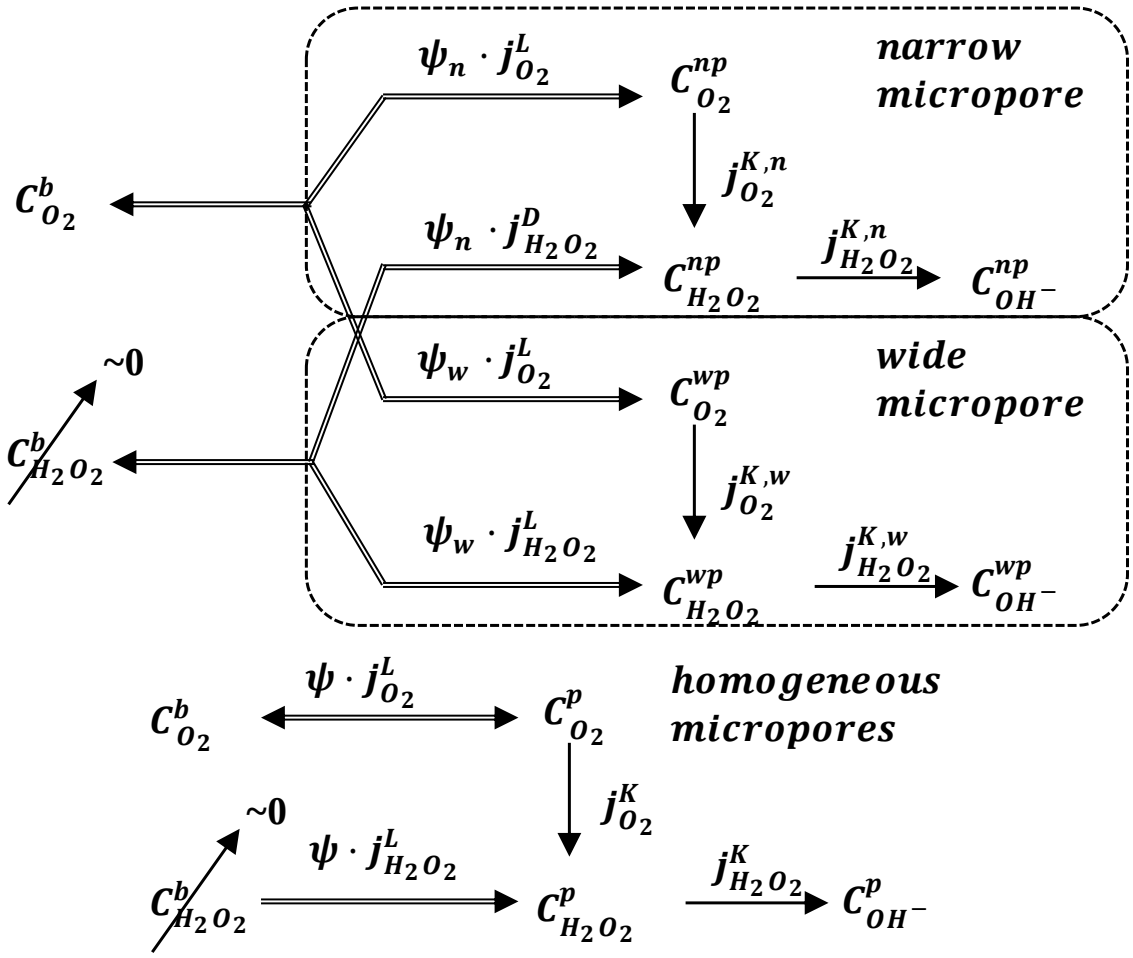

Figure 5. Schemes for the heterogeneous micropores (upper) and homogenenous micropores (bottom) models proposed for the mathematical description of the ORR mechanism of porous carbon materials

- Additionally, a model where homogeneous activity on narrow and wide micropores is assumed has been also tested. Mathematical development of this model is analogous to consider only the rate equations derived for the narrow micropores, thus making 0 all parameters and rate expressions for the wide micropores.

Figure 5 presents a graphical summary of both proposed models for estimating the ORR activity during RRDE experiments of porous carbon materials.

3.11. Application of the proposed model for predicting the ORR activity of porous carbon materials

The ORR model described in the previous section has been fitted to the LSV profiles at 1600 rpm of the porous carbon samples shown in **Figure 3**. **Figure 6** compares the experimental data with the obtained theoretical curves, while **Table 4** compiles the optimized model parameters obtained for each sample. After fitting the LSV curves, **Figure 6** demonstrates that, in general, the model is able to reproduce the ORR activity of porous carbon materials in the RRDE system. Differently, the model that considers homogeneous ORR activity in micropores produces a largest source of divergence in the number of electrons transferred at potentials higher than 0.5 V. This model cannot explain the slope changes in the number of transferred electrons (see **Figure S10**), making necessary the consideration of two H_2O_2 reaction rates of different activity (i.e. different potential dependency of the current density), like in the narrow/wide micropore model.

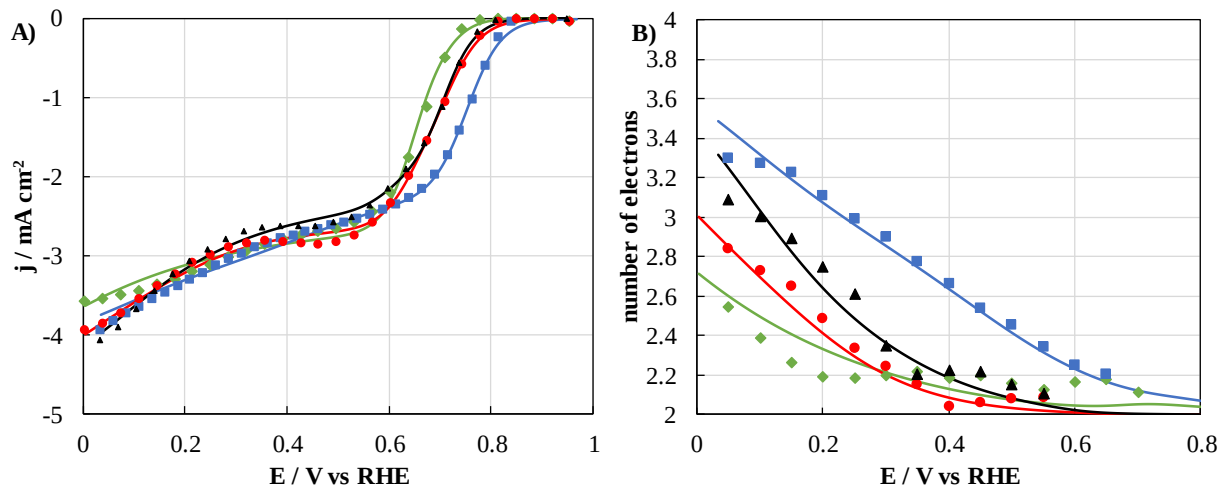

Figure 6. Experimental (dots) and modelled (lines) for A) LSV and B) number of transferred electrons profiles during ORR at 1600 rpm in 0.1 M KOH. KUA (blue), AC (red), CB (black) and XC72 (green). Scan rate: 5 mV s^{-1}.

Table 4. Optimized model parameters

Parameter	KUA	AC	CB	XC72
ψ_w	0.40	0.50	0.69	0.80
ψ_n	0.34	0.41	0.13	0.13
α_{O_2}	0.83	0.79	0.83	0.87
$k_{0,O_2}^{r,wp}$ (cm s^{-1})	$1.0\cdot10^{-8}$	$3.3\cdot10^{-9}$	$1.6\cdot10^{-9}$	$2.0\cdot10^{-9}$
$k_{0,O_2}^{r,np}$ (cm s^{-1})	$3.8\cdot10^{-9}$	$1.1\cdot10^{-9}$	$5.0\cdot10^{-10}$	$3.6\cdot10^{-10}$
$\alpha_{H_2O_2}$	0.22	0.21	0.25	0.21
$R_{H_2O_2}$	$1.8\cdot10^{-2}$	$1.4\cdot10^{-3}$	$3.4\cdot10^{-3}$	$6.9\cdot10^{-3}$
$k_{0,H_2O_2}^{r,wp}$ (cm s^{-1})	$1.7\cdot10^{-6}$	$1.3\cdot10^{-6}$	$1.2\cdot10^{-6}$	$9.5\cdot10^{-7}$

Tafel analyses have been performed for the LSV curves in the kinetically controlled region to calculate the kinetic parameters for the ORR to hydrogen peroxide. These constants have been calculated from Eqn. 13 and 18 assuming that the oxygen concentration is constant in the pores, C_{O2}^{p}, and is the same than in the bulk of the solution. The Tafel plots are shown in **Figure S10A**.

$\boldsymbol{\alpha_{O2}}$ is estimated from the slope of the linear region, being 0.82, 0.78, 0.86 and 0.89 for KUA, AC, CB and, XC72 respectively, while $\boldsymbol{k^r_{0,O_2}}$ values of $10 \cdot 10^{-9}$, $7.1 \cdot 10^{-9}$, $1.4 \cdot 10^{-9}$ and $0.25 \cdot 10^{-9}$ cm s^{-1} are determined from the Y-intercept for the same set of samples. The kinetic parameters obtained from Tafel analyses and the least square fitting of the proposed model are comparable. $\boldsymbol{\alpha_{O2}}$ and the slope of the first-wave on LSV are positively related. The proposed model delivers a slightly lower $\boldsymbol{\alpha_{O2}}$value for CB due to the decrease on the LSV slope ca. 0.6 V, **Figure 6A**, a potential region that is outside the range of data covered by the Tafel analysis (0.7-0.8V). Tafel slope of KUA, AC, CB and, XC72 are similar values (around 45-50 mV $decade^{-1}$) to those reported in previous investigations for carbon material [28].

The sum of the parameters $\psi_w + \psi_N$ (which is proportional to the effective surface area) follows the order XC72 > AC > CB > KUA. No clear relationship can be made with textural parameters derived from the N_2 adsorption isotherms. This can be explained by the different sizes of the micro and mesoporosity of the samples, that are defined in the range of a few to several nanometers, and that of the diffusion layer, which is expected to show a thickness in the range of several micrometers. Therefore, on the scale of the diffusion layer, the electrode can be considered as flat [33]. Effective surface areas lower than 1 can reflect that the surface of the disk is not fully covered for some of the samples. A similar argument has been provided for RRDE involving electrocatalytic nanoparticles [43,46]. The effective surface area of the electrodes can be also affected by the amount of Nafion® in the thin film or the particle distribution on the electrode surface [58]. Nevertheless, samples XC72, with the lowest micropore volume, and KUA, with the highest micropore volume, have the highest and the lowest ψ parameter, respectively. This is in agreement with the expected higher mass transfer limitations in highly microporous materials.

However, when the ratio $\psi_N/(\psi_N+\psi_W)$ is compared to equivalent ratios in the textural characterization, the best relationship is found with $V_{DR}^{CO2}/(V_{DR}+V_{mes})$ (R^2=0.988, **Figure 7A**). The latter parameter can be described as the ratio between narrow micropores and the total pore volume. Interestingly, the charge transfer rate constants, $k_{0,O_2}^{r,wp}$ and $k_{0,O_2}^{r,np}$, seem to be linearly connected to the N_2 and CO_2 micropore volumes of the samples, respectively (**Figure 7B and C**). However, the value of mesopore volume is unconnected, confirming that the higher amount actives sites are present in micropores.

The $\alpha_{H_2O_2}$ electron transfer coefficient values are low compared to α_{O_2} (Table 4). A similar value has been recently found for the electrocatalytic reduction of hydrogen peroxide on dispersed gold nanoparticles [59]. The low activity of undoped carbon materials towards H_2O_2 electrochemical reduction is well-known, and it is beneficial for the preparation of electrodes selective to the formation of hydrogen peroxide [48]. In the case of $R_{H_2O_2}$, the best correlation is achieved for V_{DR}^{CO2}/ V_{MES}, **Figure 7D**. Although linear trend between V_{DR}^{N2} and $k_{0,H_2O_2}^{r,wp}$ has been obtained (not included), the correlation is poorer than for the rest of analyzed parameters (R^2=0. 757). Interestingly, the ratio $k_{0,O_2}^{r,wp}/k_{L,H2O2}^{f}$ is one order of magnitude lower than that of narrow micropores, $R_{H_2O_2}=k_{0,O_2}^{r,np}/k_{D,H2O2}^{f}$, for all samples, meaning that narrow micropores have higher catalytic activity probably due to the differences in mass transfer between both type of pores that produce higher residence time for H_2O_2 within the narrow micropores.

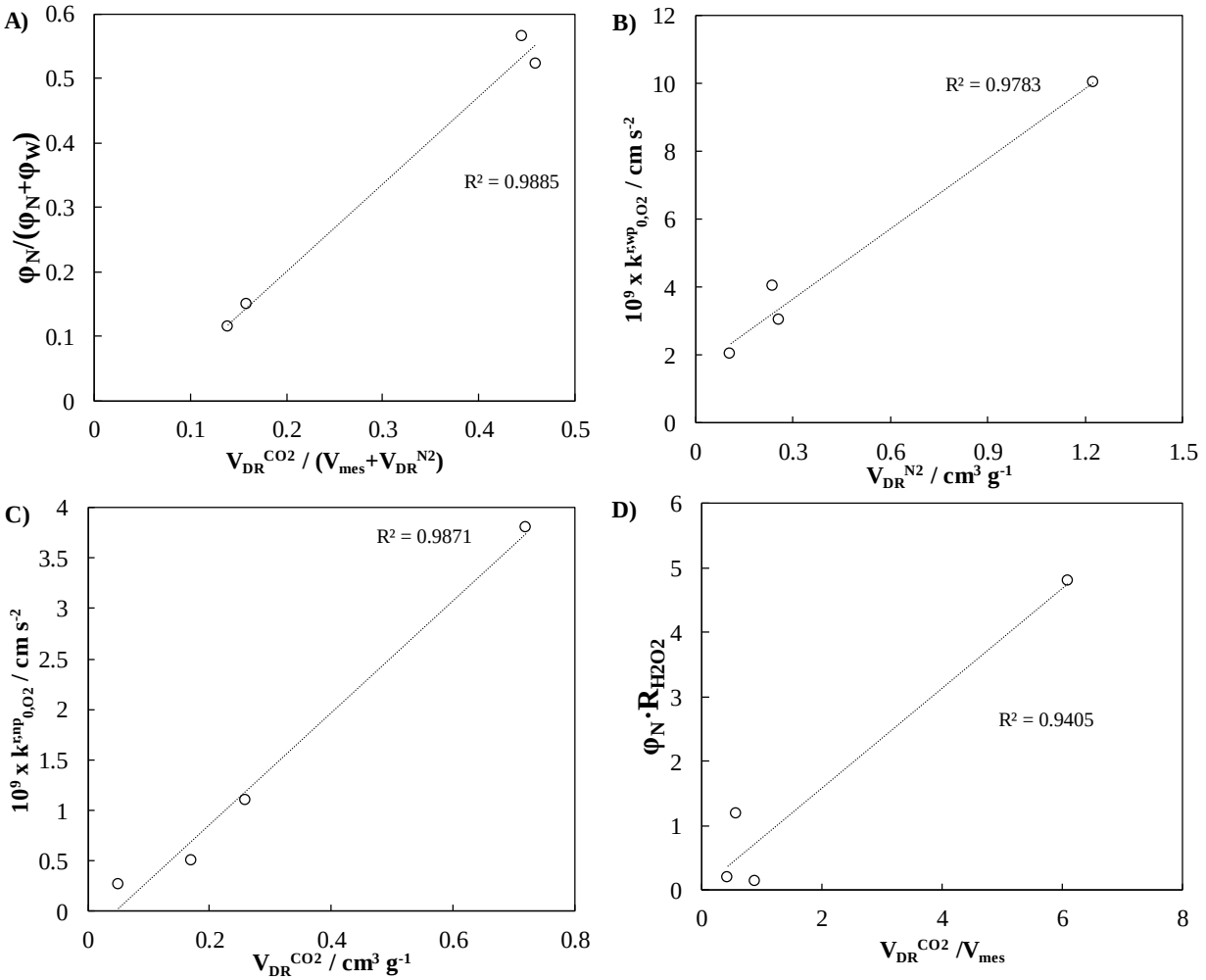

Figure 7. Relationships between textural and model parameters **A)** effective surface area ratios and narrow micropore volume. **B)** wide micropore charge transfer rate constant and micropore volume. **C)** narrow micropore charge transfer rate constant and narrow micropore volume. **D)** H_2O_2 charge transfer to mass transfer rate ratio and narrow micropore volume.

The LSV curve of KUA for 1.00 mg cm^{-2} has also been fitted to the proposed model, **Figure S11B**. The effective surface area parameters should account for the increase in the catalyst loading, owing to a larger surface area available for diffusion. The charge transfer rates could

also increase, since they include density of active sites along with other kinetic and adsorption constants, as was discussed in the definition of Eqn. 13. In consequence, the model was first applied fixing all parameters compiled in Table 4 for KUA and the $\boldsymbol{\psi_n}$ to $\boldsymbol{\psi_w}$ ratio to 0.837 (i.e. the value observed in the model fitting in Table 4 for KUA). Fixing this ratio tries to represent the independency of the textural properties of the catalysts with respect to the carbon loading. Although the only fitting parameter was $\boldsymbol{\psi_w}$, which gets a value of 0.55, the model is able to successfully describe the experimental LSV curve after the optimization step, black curve on **Figure S11B**. The effective surface area is now equal to one, what is explained by the surface the electrode fully covered by the carbon sample. An additional fitting has also been performed fixing electron transfer coefficients, while the charge transfer rates for wide micropores are optimized. Those of narrow pores are obtained from the wide pore ones by using the narrow to wide pore parameter ratios from Table 4. The new fitting results in no changes in the oxygen charge transfer rates, which seems to be independent of loading. However, the hydrogen peroxide charge transfer in wide pores increases 2.66 times, while R_{H2O2} for narrow pores increases 1.28 times, indicating that more active sites for H_2O_2 reduction are available as the loading increases. Considering that the charge transfer rate constant includes the adsorption constant, a possible explanation for the differences observed for O_2 and H_2O_2 kinetic constant rates could be that adsorption of oxygen is more favorable than adsorption of H_2O_2. Then, oxygen adsorption could be close to saturation for both catalytic loadings, having a minor impact on the charge transfer rate. Differently, the amount of adsorbed H_2O_2 could increase linearly with the catalyst loading and produce larger changes in the respective charge transfer rate. Accordingly, further experiments and more complex description of the electrode system is required for providing a more accurate description of the effect of the electrode loading.

Once the model has been verified, it can be also useful as a tool to analyze the effect of each parameter on the ORR activity of porous carbon materials. In this sense, some of the model parameters that describes KUA activity have been varied one by one and the outcomes are plotted in **Figure 8**. In first place, both ψ_N and ψ_P have been increased 20%. The LSV current on the diffusive controlled region has accordingly increased, **Figure 8A**. However, a negligible impact on the number of transferred electrons is observed (i.e. increases from 3.02 to 3.04 at 0.2 V**, Figure 8B**). The effect of shifting the pore size distribution to narrower sizes has been also explored, for what the sum of ψ_N and ψ_P has been fixed, while the ratio of $\psi_N/(\psi_N + \psi_W)$ has been increased from 0.45 to 0.60. The impact on the LSV current is low but, the number of electrons transferred increases ca. 10%, showing a value of 3.31 at 0.2V.

The effect of the charge transfer rate constants for oxygen reduction on wide and narrow pores is evaluated on **Figure 8C**. According to the previous study, a higher micropore volume should result in a charge transfer rate increase, **Figure 7**. 50% increase in the value of charge transfer rate constants for either wide or narrow micropores seems to have a small impact on the shape of the resulting LSV curve. However, detailed analyses of the kinetically controlled region, **Figure 8C**, revealed an increases of 6 and 11 mV on the onset potential (j=-0.1 mA cm^{-2}) for narrow and wide micropores, respectively. No changes in the number of electron transferred are observed, since it is governed by the occurrence of the hydrogen peroxide reduction reaction. Thus, increase of wide micropores is more effective for improving the onset potential of ORR, while shifting the PSD to narrow porosity is more effective for increasing the number of electrons transferred.

The effect of model parameters related to hydrogen peroxide has been also analyzed. The value of charge transfer rate of H_2O_2 reduction on wide pores and R_{H2O2} of narrow pores have been 3-

fold increased. The specific current on the LSV and the number of electrons increase at low potentials in the latter case and at medium potentials in the former, **Figure 8D, E**.

Lastly, the effect of increasing 5% the electron transfer coefficient for O_2 and $H2O_2$ reactions has been tested. Small increases of α_{O2} have a strong effect on the onset potential (positive shifting of 16 mV), while α_{H2O2} marginally enhances the number of electron transferred at medium and low potentials (higher currents on the diffusional controlled region on **Figure 8F**). However, this work has not found any clear relationship between electron transfer coefficients and porosity.

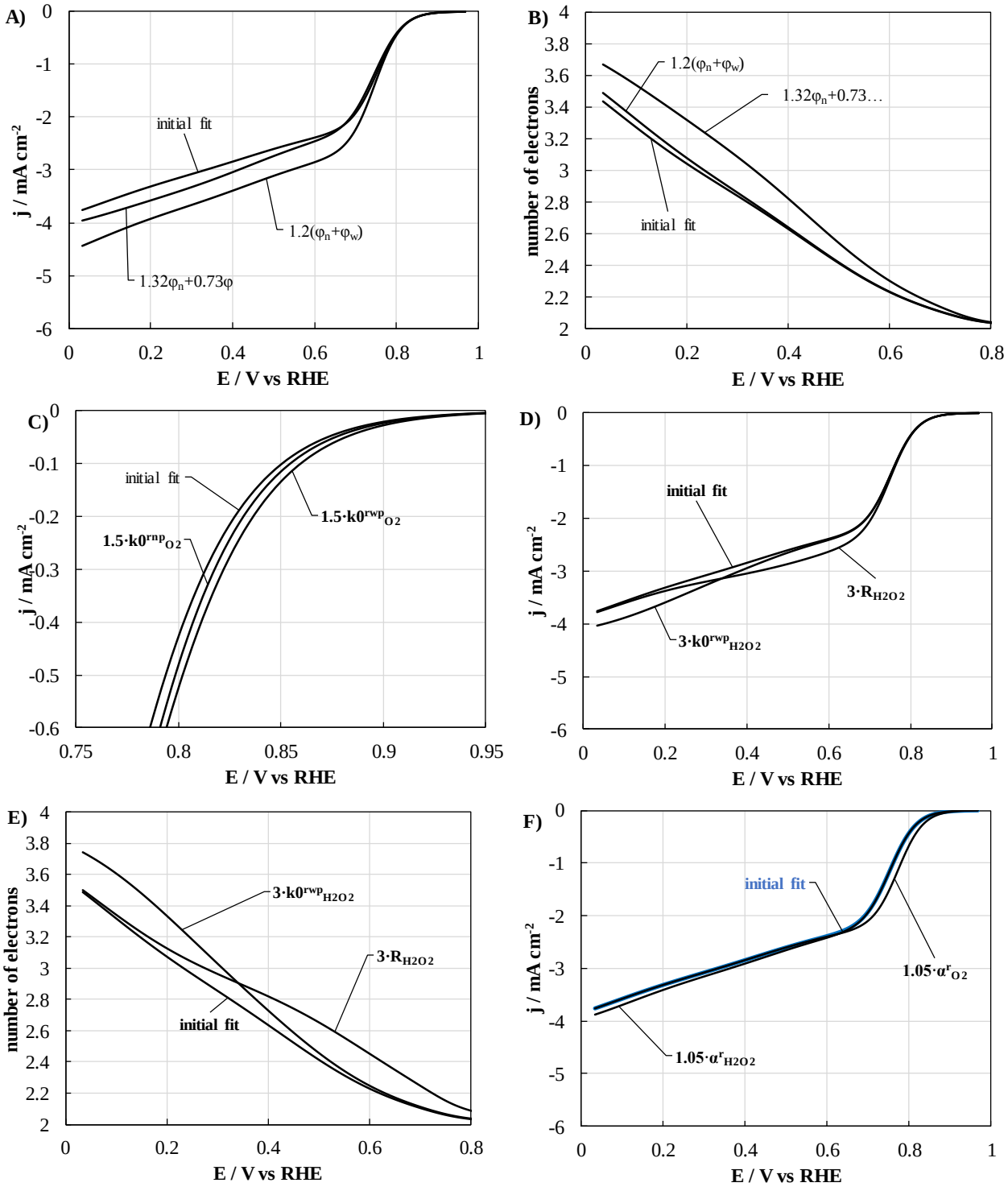

Figure 8. Effect of model parameters on the ORR activity of KUA. **A-B**) Effect of ψ_i on the LSV and number of electron transferred. **C)** Effect of $k_{0,O_2}^{r,i}$ on the simulated LSV. **D, E)** Effect of hydrogen peroxide kinetic parameters. **F)** Effect of electron transfer coefficients.

4. Conclusions

The activity of porous carbon materials in the oxygen reduction reaction in alkaline media, and in absence of any additional catalyst, is undoubtedly related to their porosity. By fully characterizing carbon materials with different pore size distribution and pore structure, we have been able to demonstrate that the ORR is accurately described by a two-wave process, where oxygen is reduced to hydrogen peroxide in a first step at intermediate potentials, while hydrogen peroxide is subsequently reduced to hydroxide at low potentials. The combination of both reactions rises the number of transferred electrons rise to intermediate values between 2 and 4.

Interestingly, the onset potentials for both reactions seems to be related to the presence of a well-developed microporosity. ORR experiments in RDE have confirmed that microporosity is certainly correlated to a high activity in this reaction, and that the presence of H_2O_2 does not interfere in the rate of the oxygen reduction reaction. In addition, ORR experiments performed with different loadings demonstrated that the amount of sample has a critical impact on the ORR activity of highly microporous materials.

A mathematical model that describes the reaction rate and number of electrons transferred during ORR and that takes into account the O_2 and H_2O_2 mass transfer rate, two consecutive reduction reactions and different activity of narrow and wide micropores has been derived from the proposed mechanism. The model gives a successful description of the ORR activity of porous carbon electrodes provided that the two types of micropores are considered, verifying the claims about the importance of microporosity on the reduction of dioxygen and of narrow microporosity on the reduction of hydrogen peroxide. The differences in adsorption potential and mass transfer between both types of pores may explain the higher activity for H_2O_2 reduction observed for

narrow micropores. This work can be a guideline for the proper analysis of ORR activity of new catalysts based on carbon materials, where the effect of porosity is frequently omitted.

ACKNOWLEDGMENT

This work was supported by the MINECO (CTQ2015-66080-R) and HEIWA NAKAJIMA FOUNDATION.

Appendix A. Supplementary data

Supplementary data related to this article can be found at

REFERENCES

[1] P. Trogadas, T.F. Fuller, P. Strasser, Carbon as catalyst and support for electrochemical energy conversion, Carbon. 75 (2014) 5–42. doi:10.1016/j.carbon.2014.04.005.

[2] L.R. Radovic, Surface Chemical and Electrochemical Properties of Carbons, in: F. Beguin, E. Frackowiak (Eds.), Carbons for Electrochemical Energy Storage and Conversion Systems, Taylor & Francis (CRC Press), Boca Raton, FL, 2010: pp. 163–219.

[3] A.L. Dicks, The role of carbon in fuel cells, Journal of Power Sources. 156 (2006) 128–141. doi:10.1016/j.jpowsour.2006.02.054.

[4] F. Jaouen, E. Proietti, M. Lefèvre, R. Chenitz, J.-P. Dodelet, G. Wu, H.T. Chung, C.M. Johnston, P. Zelenay, Recent advances in non-precious metal catalysis for oxygen-reduction reaction in polymer electrolyte fuel cells, Energy & Environmental Science. 4 (2010) 114–130. doi:10.1039/C0EE00011F.

[5] L. Dai, Y. Xue, L. Qu, H.-J. Choi, J.-B. Baek, Metal-Free Catalysts for Oxygen Reduction Reaction, Chemical Reviews. 115 (2015) 4823–4892. doi:10.1021/cr5003563.

[6] A. Morozan, B. Jousselme, S. Palacin, Low-platinum and platinum-free catalysts for the oxygen reduction reaction at fuel cell cathodes, Energy & Environmental Science. 4 (2011) 1238–1254. doi:10.1039/C0EE00601G.

[7] Y. Nie, L. Li, Z. Wei, Recent advancements in Pt and Pt-free catalysts for oxygen reduction reaction, Chem. Soc. Rev. 44 (2015) 2168–2201. doi:10.1039/C4CS00484A.

[8] C. Tamain, S.D. Poynton, R.C.T. Slade, B. Carroll, J.R. Varcoe, Development of Cathode Architectures Customized for H2/O2 Metal-Cation-Free Alkaline Membrane Fuel Cells, The Journal of Physical Chemistry C. 111 (2007) 18423–18430. doi:10.1021/jp076740c.

[9] M. Gara, R.G. Compton, Activity of carbon electrodes towards oxygen reduction in acid: A comparative study, New Journal of Chemistry. 35 (2011) 2647. doi:10.1039/c1nj20612e.

[10] H.-H. Yang, R.L. McCreery, Elucidation of the Mechanism of Dioxygen Reduction on Metal-Free Carbon Electrodes, Journal of The Electrochemical Society. 147 (2000) 3420–3428. doi:10.1149/1.1393915.

[11] T. Ikeda, M. Boero, S.F. Huang, K. Terakura, M. Oshima, J. Ozaki, Carbon alloy catalysts: Active sites for oxygen reduction reaction, Journal of Physical Chemistry C. 112 (2008) 14706–14709. doi:10.1021/jp806084d.
[12] M. Shao, Q. Chang, J.-P. Dodelet, R. Chenitz, Recent Advances in Electrocatalysts for Oxygen Reduction Reaction, Chemical Reviews. 116 (2016) 3594–3657. doi:10.1021/acs.chemrev.5b00462.
[13] J. Quílez-Bermejo, C. González-Gaitán, E. Morallón, D. Cazorla-Amorós, Effect of carbonization conditions of polyaniline on its catalytic activity towards ORR. Some insights about the nature of the active sites, Carbon. 119 (2017) 62–71. doi:10.1016/j.carbon.2017.04.015.
[14] A. Gabe, J. García-Aguilar, Á. Berenguer-Murcia, E. Morallón, D. Cazorla-Amorós, Key factors improving oxygen reduction reaction activity in cobalt nanoparticles modified carbon nanotubes, Applied Catalysis B: Environmental. 217 (2017) 303–312. doi:10.1016/j.apcatb.2017.05.096.
[15] T. Sharifi, G. Hu, X. Jia, T. Wågberg, Formation of active sites for oxygen reduction reactions by transformation of nitrogen functionalities in nitrogen-doped carbon nanotubes, ACS Nano. 6 (2012) 8904–8912. doi:10.1021/nn302906r.
[16] G.-L. Chai, Z. Hou, D.-J. Shu, T. Ikeda, K. Terakura, Active Sites and Mechanisms for Oxygen Reduction Reaction on Nitrogen-Doped Carbon Alloy Catalysts: Stone–Wales Defect and Curvature Effect, Journal of the American Chemical Society. 136 (2014) 13629–13640. doi:10.1021/ja502646c.
[17] C.V. Rao, C.R. Cabrera, Y. Ishikawa, In Search of the Active Site in Nitrogen-Doped Carbon Nanotube Electrodes for the Oxygen Reduction Reaction, The Journal of Physical Chemistry Letters. 1 (2010) 2622–2627. doi:10.1021/jz100971v.
[18] L. Zhang, Z. Xia, Mechanisms of Oxygen Reduction Reaction on Nitrogen-Doped Graphene for Fuel Cells, The Journal of Physical Chemistry C. 115 (2011) 11170–11176. doi:10.1021/jp201991j.
[19] R. Chen, H. Li, D. Chu, G. Wang, Unraveling Oxygen Reduction Reaction Mechanisms on Carbon-Supported Fe-Phthalocyanine and Co-Phthalocyanine Catalysts in Alkaline Solutions, The Journal of Physical Chemistry C. 113 (2009) 20689–20697. doi:10.1021/jp906408y.
[20] U. Tylus, Q. Jia, K. Strickland, N. Ramaswamy, A. Serov, P. Atanassov, S. Mukerjee, Elucidating Oxygen Reduction Active Sites in Pyrolyzed Metal–Nitrogen Coordinated Non-Precious-Metal Electrocatalyst Systems, The Journal of Physical Chemistry C. 118 (2014) 8999–9008. doi:10.1021/jp500781v.
[21] K. Waki, R.A. Wong, H.S. Oktaviano, T. Fujio, T. Nagai, K. Kimoto, K. Yamada, Non-nitrogen doped and non-metal oxygen reduction electrocatalysts based on carbon nanotubes: mechanism and origin of ORR activity, Energy & Environmental Science. 7 (2014) 1950–1958. doi:10.1039/C3EE43743D.
[22] C. Domínguez, F.J. Pérez-Alonso, M. Abdel Salam, S.A. Al-Thabaiti, A.Y. Obaid, A.A. Alshehri, J.L. Gómez de la Fuente, J.L.G. Fierro, S. Rojas, On the relationship between N content, textural properties and catalytic performance for the oxygen reduction reaction of N/CNT, Applied Catalysis B: Environmental. 162 (2015) 420–429. doi:10.1016/j.apcatb.2014.07.002.
[23] G.A. Ferrero, K. Preuss, A.B. Fuertes, M. Sevilla, M.-M. Titirici, The influence of pore size distribution on the oxygen reduction reaction performance in nitrogen doped carbon microspheres, Journal of Materials Chemistry A. 4 (2016) 2581–2589. doi:10.1039/C5TA10063A.
[24] J. Park, Y. Nabae, T. Hayakawa, M. Kakimoto, Highly Selective Two-Electron Oxygen Reduction Catalyzed by Mesoporous Nitrogen-Doped Carbon, ACS Catalysis. 4 (2014) 3749–3754. doi:10.1021/cs5008206.
[25] J. Maruyama, K.I. Sumino, M. Kawaguchi, I. Abe, Influence of activated carbon pore structure on oxygen reduction at catalyst layers supported on rotating disk electrodes, Carbon. 42 (2004) 3115–3121. doi:10.1016/j.carbon.2004.07.023.

[26] F. Jaouen, M. Lefèvre, J.-P. Dodelet, M. Cai, Heat-Treated Fe/N/C Catalysts for O2 Electroreduction: Are Active Sites Hosted in Micropores?, The Journal of Physical Chemistry B. 110 (2006) 5553–5558. doi:10.1021/jp057135h.
[27] M. Lefèvre, E. Proietti, F. Jaouen, J.-P. Dodelet, Iron-Based Catalysts with Improved Oxygen Reduction Activity in Polymer Electrolyte Fuel Cells, Science. 324 (2009) 71–74. doi:10.1126/science.1170051.
[28] A.J. Appleby, J. Marie, Kinetics of oxygen reduction on carbon materials in alkaline solution, Electrochimica Acta. 24 (1979) 195–202. doi:10.1016/0013-4686(79)80024-9.
[29] Y. Liu, K. Li, B. Ge, L. Pu, Z. Liu, Influence of Micropore and Mesoporous in Activated Carbon Air-cathode Catalysts on Oxygen Reduction Reaction in Microbial Fuel Cells, Electrochimica Acta. 214 (2016) 110–118. doi:10.1016/j.electacta.2016.08.034.
[30] M. Seredych, A. Szczurek, V. Fierro, A. Celzard, T.J. Bandosz, Electrochemical Reduction of Oxygen on Hydrophobic Ultramicroporous PolyHIPE Carbon, ACS Catalysis. 6 (2016) 5618–5628. doi:10.1021/acscatal.6b01497.
[31] D. Qu, Investigation of oxygen reduction on activated carbon electrodes in alkaline solution, Carbon. 45 (2007) 1296–1301. doi:10.1016/j.carbon.2007.01.013.
[32] M.A. Lillo-Ródenas, D. Lozano-Castelló, D. Cazorla-Amorós, A. Linares-Solano, Preparation of activated carbons from Spanish anthracite - II. Activation by NaOH, Carbon. 39 (2001) 751–759. doi:10.1016/S0008-6223(00)00186-X.
[33] A.J. Bard, L.R. Faulkner, Electrochemical Methods: Fundamentals and Applications, 2a., Wiley, 2001.
[34] M. Thommes, K. Kaneko, A. V. Neimark, J.P. Olivier, F. Rodriguez-Reinoso, J. Rouquerol, K.S.W. Sing, Physisorption of gases, with special reference to the evaluation of surface area and pore size distribution (IUPAC Technical Report), Pure and Applied Chemistry. 87 (2015) 1051–1069. doi:10.1515/pac-2014-1117.
[35] M.A. Lillo-Ródenas, D. Cazorla-Amorós, A. Linares-Solano, Understanding chemical reactions between carbons and NaOH and KOH: An insight into the chemical activation mechanism, Carbon. 41 (2003) 267–275. doi:10.1016/S0008-6223(02)00279-8.
[36] F. Zaragoza-Martín, D. Sopeña-Escario, E. Morallón, C.S.-M. de Lecea, Pt/carbon nanofibers electrocatalysts for fuel cells, Journal of Power Sources. 171 (2007) 302–309. doi:10.1016/j.jpowsour.2007.06.078.
[37] D. Lozano-Castelló, D. Cazorla-Amorós, A. Linares-Solano, Usefulness of CO2 adsorption at 273 K for the characterization of porous carbons, Carbon. 42 (2004) 1233–1242. doi:10.1016/j.carbon.2004.01.037.
[38] D. Cazorla-Amorós, J. Alcañiz-Monge, M.A. de la Casa-Lillo, A. Linares-Solano, CO2 As an Adsorptive To Characterize Carbon Molecular Sieves and Activated Carbons, Langmuir. 14 (1998) 4589–4596. doi:10.1021/la980198p.
[39] J. Jagiello, J.P. Olivier, 2D-NLDFT adsorption models for carbon slit-shaped pores with surface energetical heterogeneity and geometrical corrugation, Carbon. 55 (2013) 70–80.
[40] M.A. Short, P.L. Walker, Measurement of interlayer spacings and crystal sizes in turbostratic carbons, Carbon. 1 (1963) 3–9. doi:http://dx.doi.org/10.1016/0008-6223(63)90003-4.
[41] K.J.J. Mayrhofer, D. Strmcnik, B.B. Blizanac, V. Stamenkovic, M. Arenz, N.M. Markovic, Measurement of oxygen reduction activities via the rotating disc electrode method: From Pt model surfaces to carbon-supported high surface area catalysts, Electrochimica Acta. 53 (2008) 3181–3188. doi:10.1016/j.electacta.2007.11.057.
[42] U.A. Paulus, T.J. Schmidt, H.A. Gasteiger, R.J. Behm, Oxygen reduction on a high-surface area Pt/Vulcan carbon catalyst: A thin-film rotating ring-disk electrode study, Journal of Electroanalytical Chemistry. 495 (2001) 134–145. doi:10.1016/S0022-0728(00)00407-1.

[43] J. Masa, C. Batchelor-McAuley, W. Schuhmann, R.G. Compton, Koutecky-Levich analysis applied to nanoparticle modified rotating disk electrodes: Electrocatalysis or misinterpretation, Nano Research. 7 (2014) 71–78. doi:10.1007/s12274-013-0372-0.
[44] A. Bonakdarpour, M. Lefevre, R. Yang, F. Jaouen, T. Dahn, J.-P. Dodelet, J.R. Dahn, Impact of Loading in RRDE Experiments on Fe–N–C Catalysts: Two- or Four-Electron Oxygen Reduction?, Electrochemical and Solid-State Letters. 11 (2008) B105. doi:10.1149/1.2904768.
[45] M. Gara, K.R. Ward, R.G. Compton, Nanomaterial modified electrodes: evaluating oxygen reduction catalysts., Nanoscale. 5 (2013) 7304–11. doi:10.1039/c3nr01940c.
[46] K.R. Ward, M. Gara, N.S. Lawrence, R.S. Hartshorne, R.G. Compton, Nanoparticle modified electrodes can show an apparent increase in electrode kinetics due solely to altered surface geometry: The effective electrochemical rate constant for non-flat and non-uniform electrode surfaces, Journal of Electroanalytical Chemistry. 695 (2013) 1–9. doi:10.1016/j.jelechem.2013.02.012.
[47] N.P. Subramanian, X. Li, V. Nallathambi, S.P. Kumaraguru, H. Colon-Mercado, G. Wu, J.W. Lee, B.N. Popov, Nitrogen-modified carbon-based catalysts for oxygen reduction reaction in polymer electrolyte membrane fuel cells, Journal of Power Sources. 188 (2009) 38–44. doi:10.1016/j.jpowsour.2008.11.087.
[48] G. Coria, T. Pérez, I. Sirés, J.L. Nava, Mass transport studies during dissolved oxygen reduction to hydrogen peroxide in a filter-press electrolyzer using graphite felt, reticulated vitreous carbon and boron-doped diamond as cathodes, Journal of Electroanalytical Chemistry. 757 (2015) 225–229. doi:10.1016/j.jelechem.2015.09.031.
[49] M.A. de la Casa-Lillo, J. Alcañiz-Monge, E. Raymundo-Piñero, D. Cazorla-Amorós, A. Linares-Solano, Molecular sieve properties of general-purpose carbon fibres, Carbon. 36 (1998) 1353–1360. doi:10.1016/S0008-6223(98)00120-1.
[50] F. Béguin, K. Kierzek, M. Friebe, A. Jankowska, J. Machnikowski, K. Jurewicz, E. Frackowiak, Effect of various porous nanotextures on the reversible electrochemical sorption of hydrogen in activated carbons, Electrochimica Acta. 51 (2006) 2161–2167. doi:10.1016/j.electacta.2005.03.086.
[51] J. Chmiola, G. Yushin, Y. Gogotsi, C. Portet, P. Simon, P.L. Taberna, Anomalous Increase in Carbon Capacitance at Pore Sizes Less Than 1 Nanometer, Science. 313 (2006) 1760–1763. doi:10.1126/science.1132195.
[52] R. Zhou, Y. Zheng, M. Jaroniec, S.-Z. Qiao, Determination of the Electron Transfer Number for the Oxygen Reduction Reaction: From Theory to Experiment, ACS Catalysis. 6 (2016) 4720–4728. doi:10.1021/acscatal.6b01581.
[53] P.H. Matter, U.S. Ozkan, Non-metal catalysts for dioxygen reduction in an acidic electrolyte, Catalysis Letters. 109 (2006) 115–123. doi:10.1007/s10562-006-0067-1.
[54] P.H. Matter, L. Zhang, U.S. Ozkan, The role of nanostructure in nitrogen-containing carbon catalysts for the oxygen reduction reaction, Journal of Catalysis. 239 (2006) 83–96. doi:10.1016/j.jcat.2006.01.022.
[55] X. Chu, K. Kinoshita, Surface modification of carbons for enhanced electrochemical activity, Materials Science and Engineering B. 49 (1997) 53–60. doi:10.1016/S0921-5107(97)00100-1.
[56] H.A. Hansen, V. Viswanathan, J.K. Nørskov, Unifying Kinetic and Thermodynamic Analysis of 2 e– and 4 e– Reduction of Oxygen on Metal Surfaces, J. Phys. Chem. C. 118 (2014) 6706–6718. doi:10.1021/jp4100608.
[57] E. Yeager, Dioxygen electrocatalysis: mechanisms in relation to catalyst structure, Journal of Molecular Catalysis. 38 (1986) 5–25. doi:10.1016/0304-5102(86)87045-6.

[58] Y. Garsany, I.L. Singer, K.E. Swider-Lyons, Impact of film drying procedures on RDE characterization of Pt/VC electrocatalysts, Journal of Electroanalytical Chemistry. 662 (2011) 396–406. doi:10.1016/j.jelechem.2011.09.016.

[59] J.S. Jirkovský, M. Halasa, D.J. Schiffrin, Kinetics of electrocatalytic reduction of oxygen and hydrogen peroxide on dispersed gold nanoparticles, Physical Chemistry Chemical Physics. 12 (2010) 8042–8053. doi:10.1039/C002416C.

Supplementary Materials

Click here to download Supplementary Materials: J_power_sources_porosity_Supplementary_materials_DCA.docx